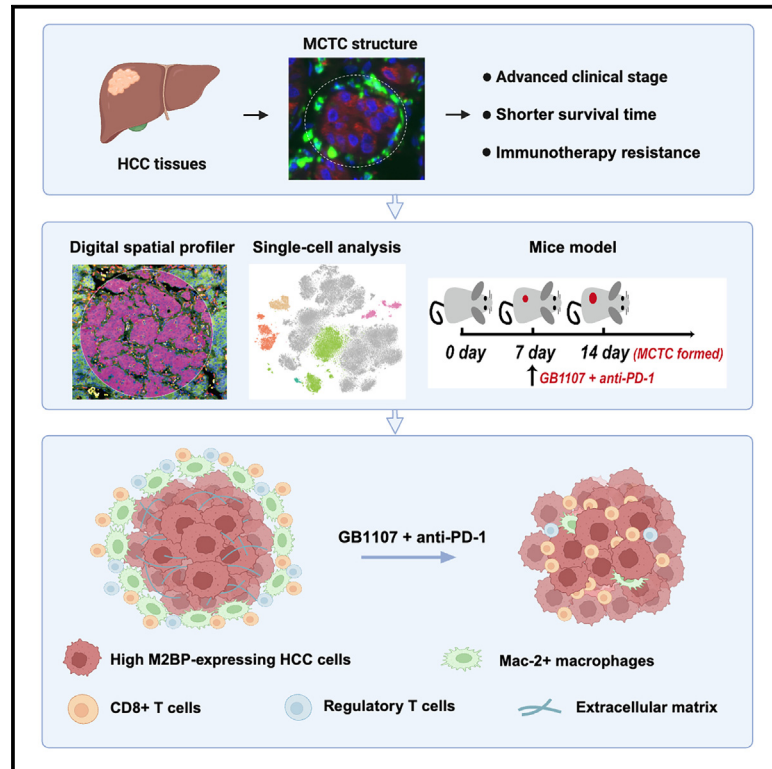


Macrophage-coated tumor cluster aggravates hepatoma invasion and immunotherapy resistance via generating local immune deprivation

Graphical abstract



Authors

Junya Ning, Yingnan Ye, Hongru Shen, ..., Fenglin Zang, Xiangchun Li, Jinpu Yu

Correspondence

lixiangchun2014@foxmail.com (X.L.), jyu@tmu.edu.cn (J.Y.)

In brief

Ning et al. identify that the MCTC structure serves as a biomarker for poor prognosis and ICI resistance in HCC, functioning by sequestering cytotoxic T cells and establishing an immunosuppressive niche. Their strategy disrupts MCTC formation by targeting M2BP, restoring T cell infiltration and potentially boosting ICI treatment efficacy.

Highlights

- MCTC structure serves as a biomarker for poor prognosis and ICI resistance in HCC
- MCTC⁺ HCC: Immunologically hot tumors with immune cells trapped outside tumor cells
- Macrophages in MCTC⁺ HCC exhibit a distinct immunosuppressive phenotype
- Anti-PD-1 and GB1107 therapy inhibits MCTC⁺ HCC growth and metastasis



Article

Macrophage-coated tumor cluster aggravates hepatoma invasion and immunotherapy resistance via generating local immune deprivation

Junya Ning,^{1,2,3,8,10} Yingnan Ye,^{1,2,3,9,10} Hongru Shen,^{3,4,10} Runjiao Zhang,^{1,2,3} Huikai Li,⁵ Tianqiang Song,⁵ Rui Zhang,^{1,2,3} Pengpeng Liu,^{1,2,3} Guidong Chen,^{1,2,3} Hailong Wang,⁶ Fenglin Zang,⁷ Xiangchun Li,^{3,4,*} and Jinpu Yu^{1,2,3,11,*}

¹Cancer Molecular Diagnostics Core, Tianjin Medical University Cancer Institute and Hospital, National Clinical Research Center for Cancer, Tianjin's Clinical Research Center for Cancer, Tianjin 300060, China

²Key Laboratory of Cancer Immunology and Biotherapy, Tianjin 300060, China

³Key Laboratory of Cancer Prevention and Therapy, Tianjin 300060, China

⁴Tianjin Cancer Institute, Tianjin's Clinical Research Center for Cancer, National Clinical Research Center for Cancer, Tianjin Medical University Cancer Institute and Hospital, Tianjin Medical University, Tianjin 300060, China

⁵Department of Liver Cancer, Tianjin Medical University Cancer Institute and Hospital, National Clinical Research Center for Cancer, Tianjin's Clinical Research Center for Cancer, Tianjin 300060, China

⁶Laboratory of Cancer Cell Biology, Tianjin Medical University Cancer Institute and Hospital, National Clinical Research Center for Cancer, Tianjin's Clinical Research Center for Cancer, Tianjin 300060, China

⁷Department of Pathology, Tianjin Medical University Cancer Institute and Hospital, National Clinical Research Center for Cancer, Tianjin's Clinical Research Center for Cancer, Tianjin 300060, China

⁸Department of Thyroid and Breast Surgery, Tianjin Union Medical Center, Tianjin 300121, China

⁹Clinical Laboratory, TEDA International Cardiovascular Hospital, Tianjin 300457, China

¹⁰These authors contributed equally

¹¹Lead contact

*Correspondence: lixiangchun2014@foxmail.com (X.L.), jyu@tmu.edu.cn (J.Y.)

<https://doi.org/10.1016/j.xcrm.2024.101505>

SUMMARY

Immune checkpoint inhibitors (ICIs) represent a promising treatment for hepatocellular carcinoma (HCC) due to their capacity for abundant lymphocyte infiltration. However, some patients with HCC respond poorly to ICI therapy due to the presence of various immunosuppressive factors in the tumor microenvironment. Our research reveals that a macrophage-coated tumor cluster (MCTC) signifies a unique spatial structural organization in HCC correlating with diminished recurrence-free survival and overall survival in a total of 572 HCC cases from 3 internal cohorts and 2 independent external validation cohorts. Mechanistically, tumor-derived macrophage-associated lectin Mac-2 binding protein (M2BP) induces MCTC formation and traps immunocompetent cells at the edge of MCTCs to induce intratumoral cytotoxic T cell exclusion and local immune deprivation. Blocking M2BP with a Mac-2 antagonist might provide an effective approach to prevent MCTC formation, enhance T cell infiltration, and thereby improve the efficacy of ICI therapy in HCC.

INTRODUCTION

Hepatocellular carcinoma (HCC) is a notably aggressive cancer with a high recurrence rate post-surgical resection.¹ Although tyrosine kinase inhibitors have been established for both primary and secondary treatments, they yield limited improvement in overall survival (OS).^{2,3} The US Food and Drug Administration's (FDA) expedited approval of immune checkpoint inhibitors (ICIs), including PD-1 and CTLA-4 antibodies, was anticipated to transform the management of advanced HCC.^{4–7} However, it did not demonstrate statistically significant improvement in OS.⁸ Therefore, it is urgent to disclose the molecular events underlying immunotherapy resistance in HCC and develop novel strategies to improve the efficacy of ICI therapy.

ICI resistance in HCC is multifaceted, but one of the most critical aspects involves the intricate interplay within the tumor microenvironment (TME).⁹ Our previous studies revealed that tumor-associated macrophages (TAMs) are prevalent in the HCC TME and have been shown to facilitate HCC cell migration and invasion through microRNA-mediated mechanisms.^{10,11} Moreover, TAMs contribute to the immunosuppressive milieu within the TME, with a higher density of TAMs correlating with poor prognosis and increased ICI resistance, as seen in various cancers.^{12–14}

Emerging evidence suggests that the spatial configuration of immune cells within tumors is pivotal for cancer progression.¹⁵ For instance, the structured interplay between cancer-associated fibroblasts and cancer cells has been implicated in the



migration of lung cancer cells and the exclusion of T cells.^{16,17} We hypothesize that in HCC, a unique spatial arrangement of TAMs could influence ICI resistance by altering the intratumoral distribution of immune cells.

In our investigation, we employed advanced high-plex molecular profiling to discover a novel spatial structure termed the macrophage-coated tumor cluster (MCTC), which we found to be indicative of poor prognosis and more aggressive HCC. Significantly, MCTC-positive (MCTC⁺) HCCs often resist ICIs due to the exclusion of intratumoral cytotoxic T cells despite being characterized as “immunologically hot” tumors. However, by inhibiting macrophage-associated lectin Mac-2 binding protein (M2BP) with a Mac-2 antagonist, we could prevent MCTC formation and restore T cell infiltration, offering a promising avenue to enhance ICI therapy efficacy in HCC.

RESULTS

Spatial heterogeneity of TAMs in HCC tissues affected the survival of patients with HCC

We delved into the spatial heterogeneity of TAMs within HCC tissues and its impact on patient survival. Employing multispectral immunofluorescence (mIF) staining on 133 HCC samples from Tianjin Medical University Cancer Institute and Hospital (TJMUCH) cohort I, we developed a TAM-based HCC classification scoring system, which is elaborated on in the [STAR Methods](#) section. We characterized four distinct spatial positioning (SP) patterns of TAMs: a low amount of TAMs dispersing among tumor cells (TAMs-LD), a low amount of TAMs surrounding a tumor cluster (TAMs-LS), a high amount of TAMs dispersing among tumor cells (TAMs-HD), and a high amount of TAMs surrounding a tumor cluster (TAMs-HS) ([Figure S1A](#)).

Comparative analysis of clinical outcomes across these TAM SP patterns revealed that patients with TAMs-HS or TAMs-HD had significantly poorer recurrence-free survival (RFS), although their OS was not markedly different when compared with those in the TAMs-LS or TAMs-LD categories. Notably, patients with the TAMs-HS pattern experienced the lowest RFS and OS rates ($p < 0.05$, [Figure 1A](#)), suggesting that the TAM SP pattern is a more critical prognostic indicator than the sheer number of intratumoral TAMs for predicting HCC recurrence and patient prognosis.

MCTC identified in HCC tissues is a valuable predictor of recurrence and is related to aggressive pathological features

Utilizing whole-slide imaging, we coined the term MCTC to describe the SP pattern observed in TAMs-HS patients, which was prevalent across various sites in the tissue sections ([Figure S1B](#)). With StrataQuest software, we delineated the perimeters of tumor clusters and quantified TAMs within incremental distances from the tumor edge. Our analysis pinpointed the 0–10 μm zone as critically influencing RFS and OS ($p < 0.05$, [Figure 1B](#)), aligning with prior findings that a 10 μm range is indicative of direct macrophage-tumor cell interaction.

We counted the amount of TAMs within a 0–10 μm distance outward from the edge of tumor clusters and calculated the ratio of TAMs vs. tumor cells (M:T) in the MCTC. The result showed that the optimal cutoff amount of TAMs was 4 and the optimal

cutoff ratio of M:T was 1:2. Combination of the two parameters displayed a better efficiency in predicting the recurrence of HCC, which yielded 74.4% accuracy ($p = 0.0013$) ([Table S1](#)). Therefore, we defined MCTC⁺ HCC as the HCC cases with more than one tumor cluster surrounding at least 4 TAMs at an M:T ratio larger than 1:2.

Upon assessing MCTC structures in 253 HCC samples from two distinct TJMUCH cohorts, nearly one-third were classified as MCTC⁺ (51/133 in TJMUCH cohort I and 46/120 in TJMUCH cohort II). These patients exhibited markedly reduced RFS and OS in comparison to their MCTC⁻ counterparts ($p < 0.05$, [Figure 1C](#)). MCTCs were significantly linked to adverse RFS and OS via Cox univariate analysis and were further validated as an independent prognostic factor in multivariate models ($p < 0.05$, [Table S2](#)). Clinically, MCTCs correlated with larger tumors, increased microvascular invasion and satellite nodules, and higher Barcelona-Clinic Liver Cancer (BCLC) grades. The distant metastasis rate of MCTC⁺ patients was significantly higher than those of MCTC⁻ patients ([Table S3](#)). It is worth noting that the prognosis of MCTC⁺ patients was worse than MCTC⁻ patients for both early- and advanced-stage HCC ([Figure S2A](#)). These results suggested that MCTCs are not only associated with the enhanced aggressiveness and metastatic potential of HCC cells but also played a pivotal role in driving the malignant progression of HCC.

To further substantiate the prognostic value of MCTC, we extended our analysis to additional cohorts, including an in-house cohort (TJMUCH III) and two external cohorts from different medical centers (Xinchao and Yaxiang cohorts). Consistently, approximately one-third of these patients were MCTC⁺ (26/64 in TJMUCH cohort III, 59/175 in Xinchao cohort, and 23/80 in Yaxiang cohort), and they experienced significantly worse survival outcomes ($p < 0.05$, [Figures 1D](#), [S2B](#), and [S2C](#)). Univariate and multivariate Cox regression analyses conducted across external cohorts have substantiated the role of MCTC as a risk factor. These analyses also confirmed MCTC as an independent prognostic marker for RFS and OS in the Xinchao cohort, as well as for OS in the Yaxiang cohort ([Tables S4](#) and [S5](#)). This reinforces the role of MCTC as a biomarker for aggressive HCC and as a potential target for therapeutic strategies.

MCTC predicted poor response to ICI therapy in patients with HCC

The predictive capacity of MCTC for ICI response was evaluated in patients with HCC considering the dense TAM infiltration in MCTC⁺ HCC tissues. Through a comprehensive immunomodulatory gene signature analysis¹⁸ conducted on 64 HCC samples from TJMUCH cohort III, it was revealed that MCTC⁺ HCC samples had significantly lower immunomodulatory signature scores compared to MCTC⁻ samples ([Figure 2A](#)). This suggested a potential poor response to ICI therapy in MCTC⁺ HCC.

Clinical data from 28 patients with HCC undergoing ICI therapy (TJMUCH cohort IV) showed a marked difference in the objective response rate between MCTC⁺ and MCTC⁻ groups (28.57% vs. 76.19%, respectively) ([Figure 2B](#)), indicating ICI resistance in MCTC⁺ HCC. A further investigation into the distribution of immune cells revealed a significant increase of CD8⁺ T cells in MCTC⁺ samples. However, these T cells were primarily

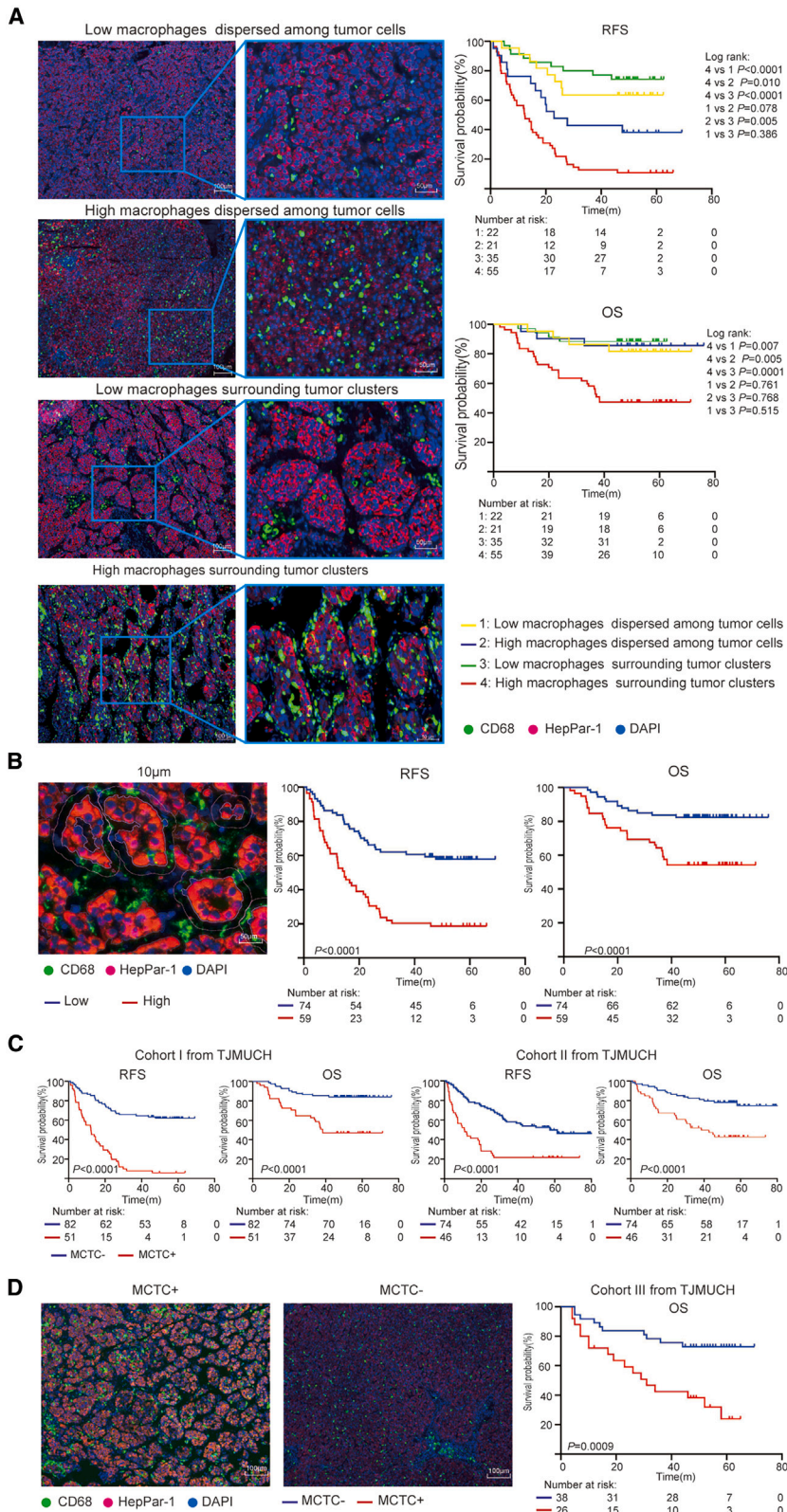


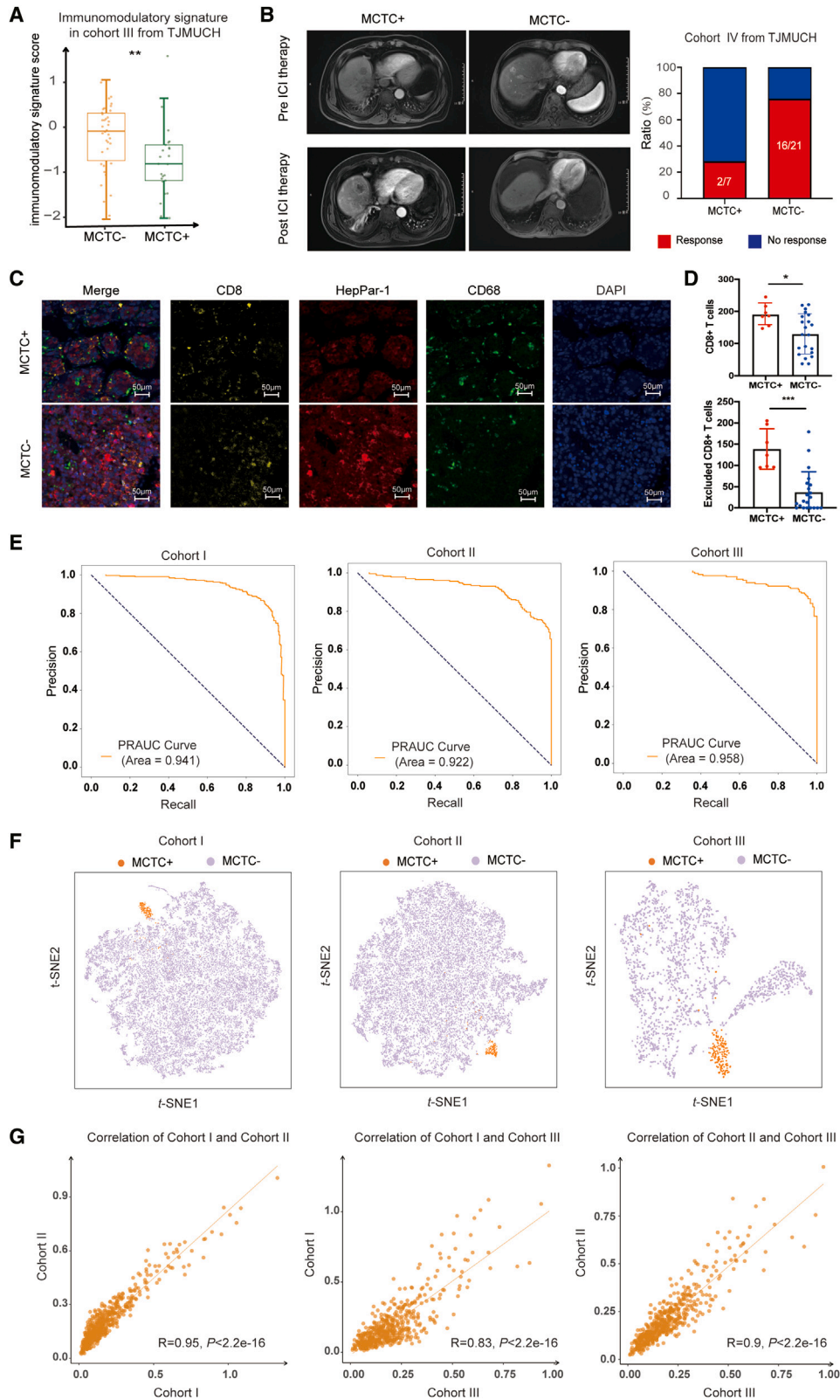
Figure 1. MCTC identified in HCC tissues is a valuable predictor of recurrence and is related to aggressive pathological features

(A) Representative images (left) alongside RFS and OS Kaplan-Meier curves (right) for four distinct spatial patterns of TAMs in HCC tissues from TJMUCH cohort I (high-magnification scale bars: 50 μ m; low-magnification scale bars: 100 μ m).

(B) Representative images (left) alongside RFS and OS Kaplan-Meier curves (right) for TAMs located within 0–10 μ m from tumor clusters in HCC tissues from TJMUCH cohort I (scale bars: 50 μ m). The methodologies used for identifying tumor clusters and for the quantitative analysis of TAMs in the same area as the representative images are detailed in Figure S1A.

(C) Comparative RFS and OS Kaplan-Meier curves for MCTC⁺ vs. MCTC⁻ HCC patients in cohort I (left) and cohort II (right) from TJMUCH.

(D) Representative images (left) alongside OS Kaplan-Meier curves (right) for MCTC⁺ vs. MCTC⁻ HCC patients in cohort III from TJMUCH (scale bars: 100 μ m).



(legend on next page)

located around MCTCs and not within the tumor nests, unlike the MCTC⁻ samples where CD8⁺ T cells penetrated the tumor core (Figures 2C and 2D). This pattern suggests a key role of TAMs in MCTCs in sequestering cytotoxic T cells and thereby diminishing the effectiveness of ICI therapy.

Advancing our analysis, we employed deep learning artificial intelligence (AI) to characterize MCTC structures in imaging. 323 MCTC⁺ images with IF staining and 25,061 MCTC⁻ images obtained from TJMUCH cohort I were used as the training set. 230 MCTC⁺ images and 18,690 MCTC⁻ images from TJMUCH cohort II were used as validation set I. Besides that, 166 MCTC⁺ images and 2,179 MCTC⁻ images from TJMUCH cohort III were used as validation set II. A deep convolutional neural network (DCNN) was trained using IF-stained images from TJMUCH cohort I and validated with cohorts II and III. The DCNN model showed high precision in identifying MCTC⁺ images, with precision-recall area under the curve values of 0.941 (95% confidence interval [CI] = 0.924–0.956) for the training set, 0.922 (95% CI = 0.900–0.944) for validation set I, and 0.958 (95% CI = 0.940–0.974) for validation set II (Figure 2E). t-Distributed stochastic neighbor embedding (t-SNE) analysis further distinguished MCTC⁺ from MCTC⁻ images (Figure 2F), with strong correlations in MCTC⁺ features across all sets, as evidenced by Pearson correlation coefficients of 0.95, 0.83, and 0.90 for the respective comparisons (Figure 2G). These findings support the notion that MCTC is reliably identifiable through image clustering and suggest that AI could be a powerful tool in future clinical settings to identify MCTCs and predict ICI therapy responses.

MCTC⁺ HCC was characterized as having immunologically hot tumors infiltrated by abundant active immunocompetent cells trapped outside cancer cells

In our exploration of the molecular dynamics underpinning the metastasis facilitated by MCTCs in HCC, we utilized NanoString's GeoMx Digital Spatial Profiler to discern the expressional variances between MCTC⁺ and MCTC⁻ regions. Molecular distinctions between macrophage-dominated and tumor-cell-dominated compartments were defined using fluorescence-labeled antibodies targeting CD68 and panCK, enabling precise microdissection (Figure S3A). A total of 1,812 genes and 55 pro-

teins were detected in CD68⁺ macrophage and panCK⁺ tumor cell compartments (Table S6).

In the CD68⁺ macrophage compartments of MCTC⁺ regions, we identified an upregulation of immune-related pathways at the mRNA level, such as antigen presentation, costimulatory, cytotoxicity, immune cell adhesion and migration, interferon signaling, and interleukin-6/JAK/STAT3 signaling, compared to MCTC⁻ regions (Figure 3A). At the protein level, enhanced expression of T cell markers CD3 and CD8 was noted (Figure S3B), suggesting a robust infiltration of active immunocompetent cells in MCTC⁺ vs. MCTC⁻ HCC. Gene Ontology (GO) pathway analysis further confirmed the engagement of immune-related pathways in MCTC⁺ HCC samples (Figure 3B), indicating a heightened immune response compared to MCTC⁻ samples. XCell analysis corroborated these findings, showing a significant increase in immunocompetent cells like CD4⁺ memory T cells, CD8⁺ T cells, and dendritic cells (DCs) in MCTC⁺ HCC (Figure 3C).

Further comparisons at the mRNA level within CD68⁺ macrophage-predominant areas of interest (AOIs) revealed a higher presence of immune cells, including CD8⁺ T cells and cytotoxic cells, compared to panCK⁺ tumor-cell-dominated AOIs (Figure 3D). Protein-level analysis showed an increase in cytotoxic and exhausted T cells in CD68⁺ macrophage-dominated AOIs (Figure S3C). This observation led us to postulate that in MCTC⁺ HCC, cytotoxic T cells are strategically relegated to the tumor periphery by TAMs, effectively hampering their direct anti-tumoral activities. To corroborate this hypothesis, we employed mIF to analyze the average distances between CD68⁺ macrophages, CD68⁺CD163⁺ M2-polarized macrophages, and tumor-infiltrating T cells, including CD8⁺ and Foxp3⁺ T cells. We discovered that in MCTC⁺ tissues, both CD8⁺ T cells and Foxp3⁺ T cells were significantly closer to CD68⁺ macrophages and CD68⁺CD163⁺ M2-polarized macrophages compared to their counterparts in MCTC⁻ tissues (Figures 3E–3H).

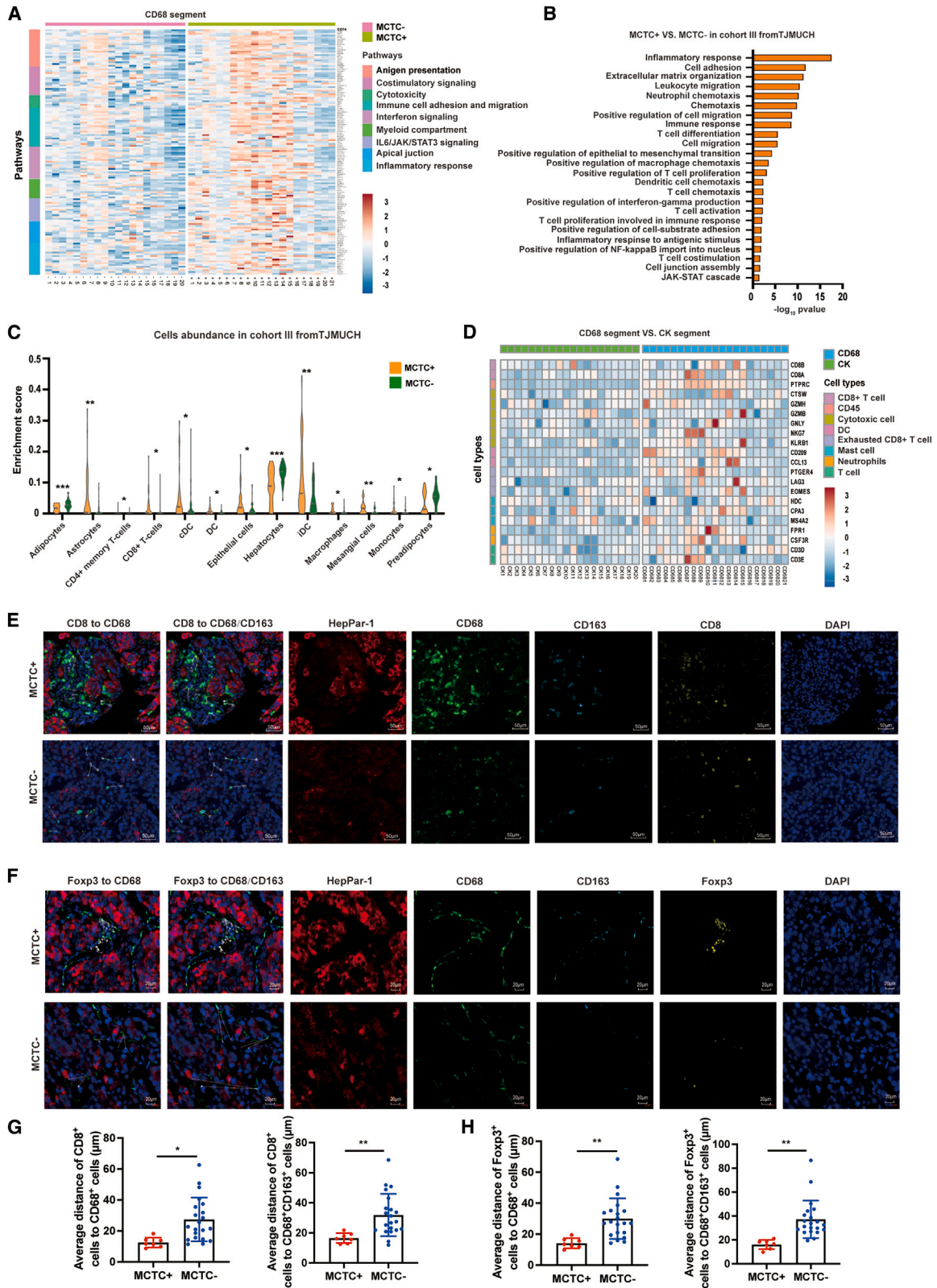
Collectively, these results suggested that although MCTC⁺ HCC tissues were characterized as immunologically hot tumors, a multitude of immunologically competent cells were sequestered outside the MCTC, impeding their infiltration into the tumor core.

Macrophages in MCTC⁺ HCC exhibited a distinct immunosuppressive and pro-tumorigenic phenotype

In our exploration of the functional and phenotypic landscape of macrophages within MCTCs, single-cell RNA sequencing

Figure 2. MCTCs predicted poor response to ICI therapy in HCC patients

- (A) Comparison of immunomodulatory gene signatures between MCTC⁺ and MCTC⁻ groups in cohort III from TJMUCH.
 (B) Pre- and post-ICI treatment computed tomography (CT) images of patients with MCTC⁺ or MCTC⁻ status alongside an analysis of the correlation between MCTC presence and response to ICI therapy in cohort IV from TJMUCH.
 (C) Immunofluorescence imaging depicting the distribution of CD8⁺ T cells in MCTC⁺ and MCTC⁻ HCC tissues (scale bars: 50 μm).
 (D) Quantification analysis of total CD8⁺ T cells (top) and excluded CD8⁺ T cells (bottom) in MCTC⁺ and MCTC⁻ samples of TJMUCH cohort IV.
 (E) Performance of a deep learning model in differentiating MCTC⁺ from MCTC⁻ images demonstrated by precision-recall area under the curve (PRAUC) values in training and validation datasets from HCC tissues of TJMUCH cohorts. Cohort I was utilized for training (left), while cohort II (center) and cohort III (right) were employed for validation.
 (F) t-Distributed stochastic neighbor embedding (t-SNE) scatterplots representing the separation of MCTC⁺ and MCTC⁻ images in the training set and two validation sets, with orange dots denoting MCTC⁺ images and lavender dots representing MCTC⁻ images. Cohort I is displayed on the left, cohort II in the center, and cohort III on the right.
 (G) Pearson correlation analysis assessing the features of MCTC⁺ images across the training and validation sets. The left plot depicts the correlation scatter diagram between cohort I and cohort II, and the center plot shows the correlation between cohort I and cohort III and the right plot between cohort I and cohort III. Data are represented as mean ± SEM. **p* < 0.05, ***p* < 0.01, and ****p* < 0.001.



(legend on next page)

(scRNA-seq) granted us insight into the cellular composition of three MCTC⁺ and three MCTC⁻ HCC cases. Utilizing marker gene analysis, we successfully categorized the profiled cells into tumor cells, T cells, macrophages, fibroblasts, endotheliocytes, and B cells (Figures 4A and 4B). Moreover, we distinguished four macrophage clusters with distinct characteristics. Notably, macrophages within MCTC⁺ tissues were predominantly accumulated in cluster 2, signaling a specialized macrophage phenotype within MCTC⁺ tissues (Figure 4C). Drawing upon the TAM characteristics derived from scRNA-seq data as summarized by Ma et al.,¹⁹ we analyzed our macrophage phenotypes and observed that macrophages in cluster 2 distinctly exhibited signatures associated with lipid-associated (LA-TAMs), immune-regulatory (Reg-TAMs), and pro-angiogenic (Angio-TAMs) phenotypes (Figure 4D). These macrophages are implicated in oncogenesis through their roles in facilitating immune evasion, providing nutrients, and meeting the metabolic needs of cancer cells. Comparative analysis revealed a significant upregulation of these TAM subsets in macrophages of MCTC⁺ HCC tissues pointing to their heightened pro-tumorigenic potential (Figure 4E). However, no significant difference was observed in other TAM subtypes between MCTC⁺ and MCTC⁻ tissues (Figures S4A and S4B). GO analysis on macrophages of cluster 2 highlighted the activation of pathways that underscore their complex interplay within the TME, such as those involved in inhibiting T cell proliferation and fostering regulatory T cell (Treg) differentiation alongside promoting cell migration, angiogenesis, and adhesion (Figure 4F). These results suggested that macrophages in MCTC⁺ HCC exhibited a distinct immunosuppressive and pro-tumorigenic phenotype.

Our investigation also illuminated the pivotal role of Trem2, primarily expressed in tumor-infiltrating macrophages and recognized for its immunosuppressive impact and its significant association with ICI resistance.²⁰ Trem2⁺ macrophages were predominantly observed in cluster 2 (Figure 4G) and were more abundant in MCTC⁺ tissues, as substantiated by mIF staining in TJMUCH cohort IV (Figure 4H). Additionally, our analysis extended to Tregs (marked by Foxp3) and T cells with an exhausted phenotype (marked by CD39) within TJMUCH cohort IV tissues, which play a significant role in modulating immune responses within the TME. The results demonstrated that these cells were markedly elevated in MCTC⁺ tissues and exhibited a positive correlation with the proportion of Trem2⁺ macrophages

(Figures S4C–S4F). The results implied that Trem2⁺ macrophages in MCTC⁺ tissues might trigger the immunosuppressive microenvironment and diminish the anti-tumor efficacy of cytotoxic T cells by inducing Treg amplification and T cell exhaustion.

Tumor-derived M2BP reinforced the chemotaxis and cell-to-cell adhesion to induce MCTC formation *in vitro* and *in vivo*

Investigating the interplay between tumor cells and the microenvironment in MCTC⁺ HCC, we found that certain signaling pathways crucial for immune cell adhesion and migration were significantly activated in panCK⁺ compartments of MCTC⁺ regions compared to MCTC⁻ regions (Figure 5A). The mRNA expression of adhesion-related genes (ITGB2, FLNA, COL1A1, COL1A2, COL3A1, and COL4A1) and proteins (fibronectin and SMA) was notably higher in MCTC⁺ regions (Figure S5A), suggesting stronger cell-cell adhesion within MCTC⁺ regions.

To delve deeper into the molecular mechanisms of cell-cell adhesion in MCTC⁺ HCC, whole-genome gene expression profiling of 64 HCC samples from TJMUCH cohort III was conducted. This revealed a marked increase in the expression of LGALS3BP (M2BP) (Figure 5B). Interactions of M2BP with proteins such as fibronectin were suggested through STRING database analysis (Figure S5B). IF confirmed that M2BP expression was restricted to HepPar-1⁺ cells, signifying its origin from cancer cells (Figure S5C). Immunohistochemistry corroborated that M2BP expression was significantly higher in MCTC⁺ HCC tissues than in MCTC⁻ tissues ($p < 0.0001$, Figure 5C).

Functional assays revealed that M2BP silencing in a high-metastatic HCC cell line (MHCC97H) reduced macrophage chemotaxis and adhesion, while M2BP overexpression in a low-metastatic line (MHCC97L) enhanced these properties. The Mac-2 antagonist GB1107 effectively inhibited these processes, particularly in M2BP-overexpressing cells (Figures 5D–5F and S5D–S5G).

In vivo studies using M2BP overexpressing Hepa1-6 cells (Hepa1-6^{M2BP^{hi}}) in mice models mirrored these findings. M2BP overexpression promoted MCTC formation and CD8⁺ T cell sequestration at MCTC peripheries, while treatment with the Mac-2 antagonist GB1107 effectively disrupted this process and reduced tumor burden and metastasis (Figures 6A–6C). Utilizing flow cytometry, we scrutinized the phenotypic profiles of

Figure 3. MCTC⁺ HCC was characterized as having immunologically hot tumors infiltrated by abundant active immunocompetent cells trapped outside the cancer cells

- (A) Heatmap displaying the differential gene expression and pathway enrichment within CD68⁺ compartments in MCTC⁺ regions and MCTC⁻ regions as revealed by highly multiplexed spatial profiling of RNAs utilizing NanoString GeoMx DSP technology.
- (B) The GO pathway enrichment analysis demonstrating pathways upregulated in the MCTC⁺ group compared to the MCTC⁻ group based on the analysis of 64 HCC transcriptomes from TJMUCH cohort III.
- (C) Violin plots display the cell-type enrichment analysis between the MCTC⁺ group and MCTC⁻ group based on 64 HCC transcriptomes from TJMUCH cohort III.
- (D) Heatmap illustrating the cell types within CD68 AOs and CK AOs utilizing RNA profiling.
- (E) Representative immunofluorescence images showcasing HepPar-1, CD68, CD163, and CD8 in MCTC⁺ and MCTC⁻ HCC tissues in MCTC⁺ and MCTC⁻ HCC tissues from TJMUCH cohort IV (scale bars: 50 μ m).
- (F) Representative immunofluorescence images showcasing HepPar-1, CD68, CD163, and Foxp3 in MCTC⁺ and MCTC⁻ HCC tissues in MCTC⁺ and MCTC⁻ HCC tissues from TJMUCH cohort IV (scale bars: 20 μ m).
- (G) Analysis of the average distances between CD8⁺ T cells and CD68⁺ macrophages (left) as well as CD68⁺CD163⁺ M2-polarized macrophages (right) in MCTC⁺ and MCTC⁻ HCC tissues from TJMUCH cohort IV.
- (H) Analysis of the average distances between Foxp3⁺ T cells and CD68⁺ macrophages (left) as well as CD68⁺CD163⁺ M2-polarized macrophages (right) in MCTC⁺ and MCTC⁻ HCC tissues from TJMUCH cohort IV.
- Data are represented as mean \pm SEM. * $p < 0.05$, ** $p < 0.01$, and *** $p < 0.001$.

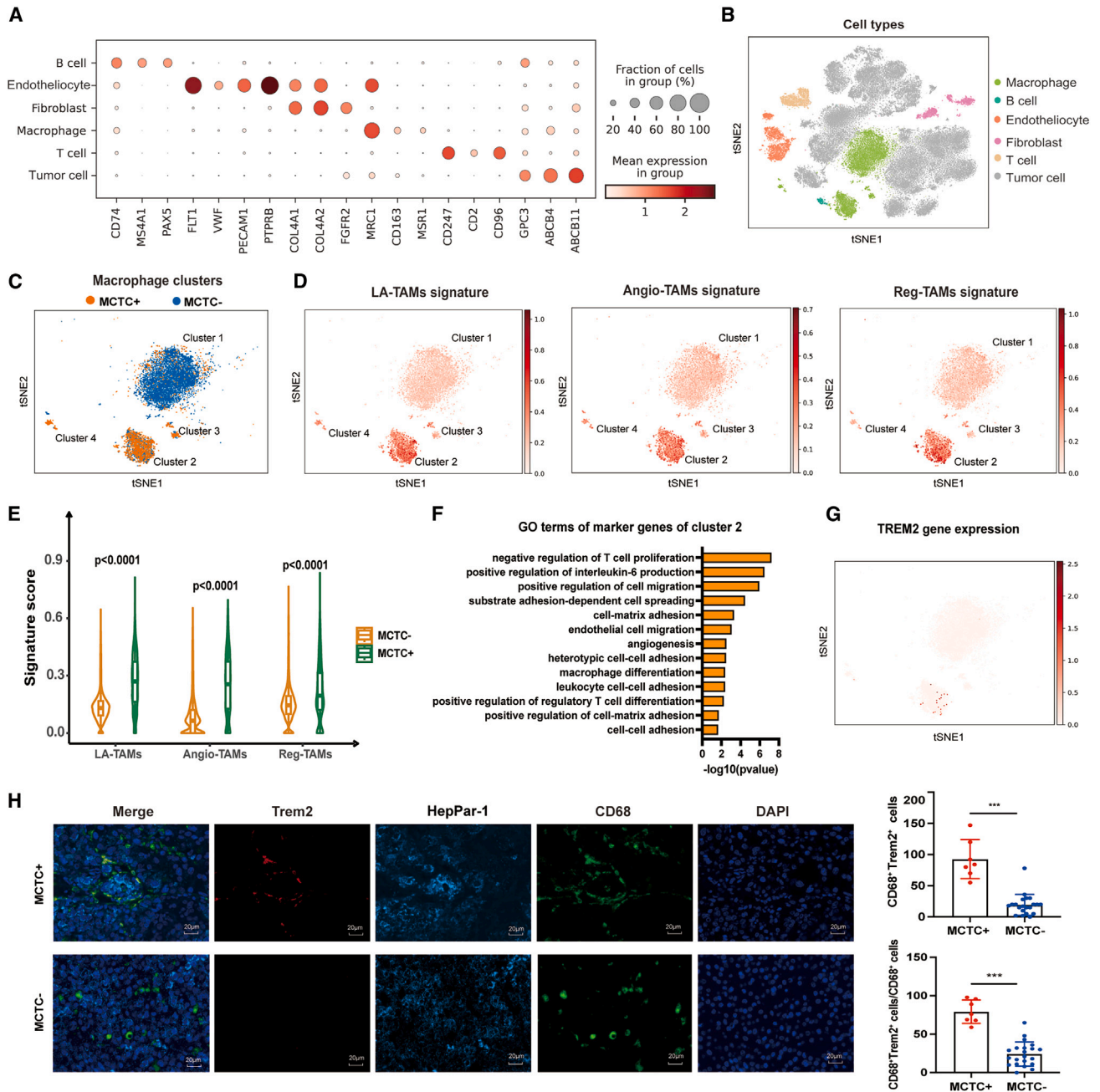


Figure 4. Macrophages in MCTC⁺ HCC exhibited a distinct immunosuppressive and pro-tumorigenic phenotype

(A) Bubble chart delineating marker genes for various cellular identities, as identified by scRNA-seq data, encompassing tumor cells, T cells, macrophages, fibroblasts, endotheliocytes, and B cells.

(B) t-SNE map derived from scRNA-seq data showcasing the diverse cellular clusters within the samples, encompassing tumor cells, T cells, macrophages, fibroblasts, endotheliocytes, and B cells, each distinctly grouped by their unique gene expression profiles.

(C) t-SNE visualization of macrophage distribution patterns in MCTC⁺ and MCTC⁻ HCC tissues based on scRNA-seq data.

(D) t-SNE map depicting the signature scores of LA-TAMs, Angio-TAMs, and Reg-TAMs derived from scRNA-seq data, with color indicating the signature score.

(E) Violin plots of the signature scores of LA-TAMs, Angio-TAMs, and Reg-TAMs in macrophages from MCTC⁺ and MCTC⁻ HCC tissues based on scRNA-seq data.

(F) GO pathway enrichment analysis of marker genes in cluster 2 based on scRNA-seq data.

(G) t-SNE map showing the expression of Trem2 in macrophage cluster on scRNA-seq data.

(H) Immunofluorescence images displaying the distribution of Trem2 protein expression in MCTC⁺ and MCTC⁻ HCC tissues (left, scale bars: 20 μm) along with an analysis of the quantity and proportion of Trem2⁺ macrophages (right) in MCTC⁺ and MCTC⁻ HCC tissues from TJMUCH cohort IV.

Data are represented as mean \pm SEM. * $p < 0.05$, ** $p < 0.01$, and *** $p < 0.001$.

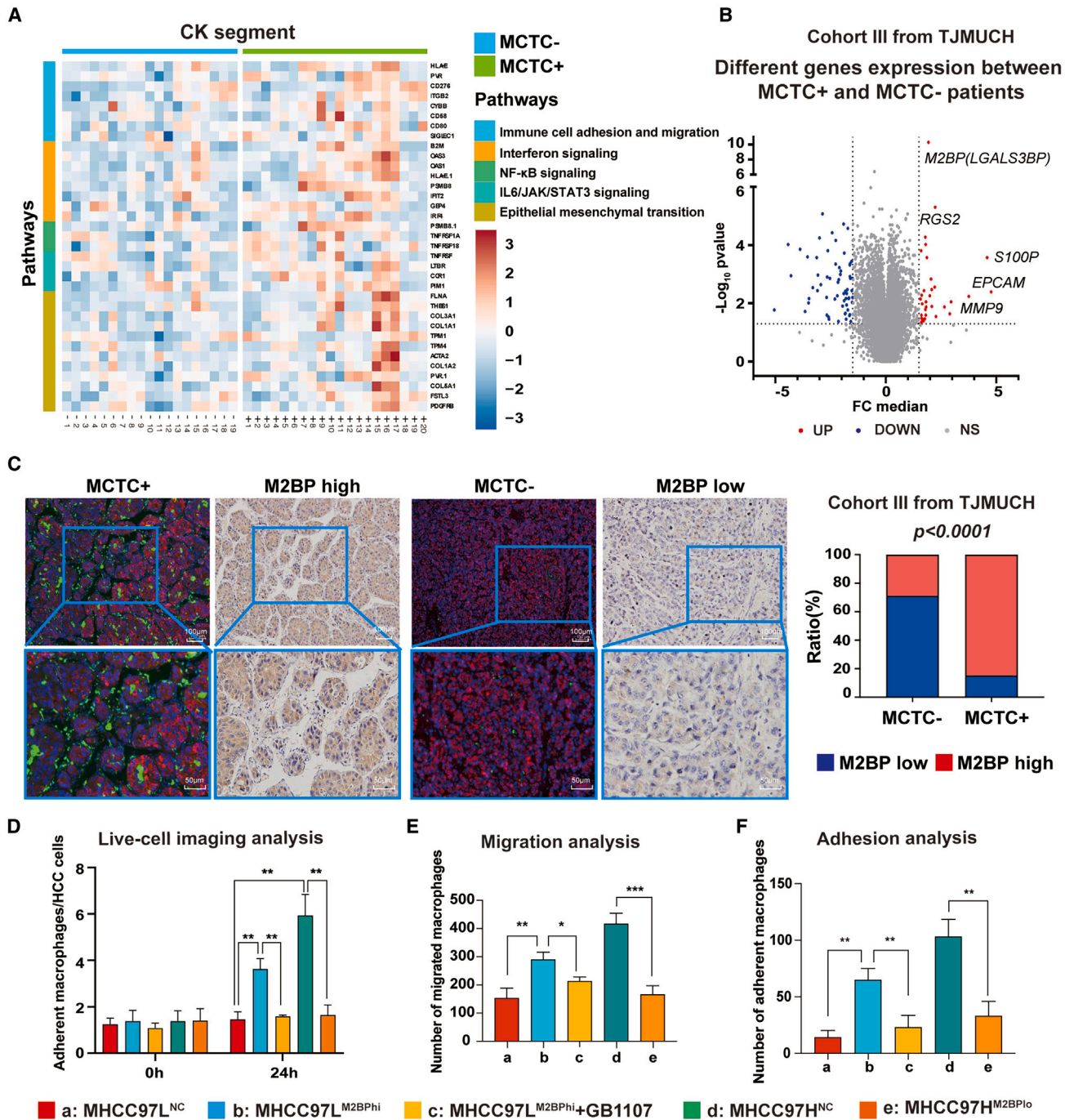


Figure 5. Tumor-derived M2BP reinforced the chemotaxis and cell-to-cell adhesion to induce MCTC formation

(A) Heatmap depicting the differential gene expression and pathway enrichment within panCK⁺ compartments of MCTC⁺ and MCTC⁻ regions as determined by highly multiplex spatial profiling of RNAs.

(B) Volcano plot illustrating differential gene expression between MCTC⁺ and MCTC⁻ groups in TJMUHC cohort III.

(C) Representative immunohistochemistry (IHC) images showcasing M2BP expression and corresponding immunofluorescence images for MCTC status (left) and correlation analysis between M2BP expression and MCTC (right) in HCC tissues from TJMUHC cohort III (high-magnification scale bars: 50 μ m; low-magnification scale bars: 100 μ m).

(D) MHCC97L cells were subjected to stable overexpression of M2BP and treated with GB1107, while MHCC97H cells underwent stable knockdown of M2BP. Live-cell imaging analysis displayed the proportion of macrophages adhering to these treated tumor cells at 0 and 24 h. Data are represented as mean \pm SD (n = 3 independent experiments).

(legend continued on next page)

macrophages and T cells within the TME of Hepa1-6^{M2BPhi}-driven subcutaneous tumors. Compared to controls, there was a pronounced increase in Mac-2⁺ macrophages and M2-polarized macrophages alongside a corresponding decrease in M1-polarized macrophages. Notably, there was a significant augmentation in the population of Trem2⁺ M2-polarized macrophages. Despite the stable numbers of CD4⁺ and CD8⁺ T cells, we observed a significant upsurge in Tregs and T cells presenting with widely recognized markers of exhaustion, namely CD39, PD-1, and LAG-3. Conversely, GB1107 treatment drastically reduced Mac-2⁺ macrophage infiltration, reversed M2 polarization, and diminished the Trem2⁺ M2 subset. This treatment also notably decreased the population of Tregs and exhausted T cells, implying a reinvigoration of the immune response (Figure 6D).

These results delineated the critical involvement of M2BP in facilitating the formation of MCTC by enhancing Mac-2⁺ macrophage chemotaxis and adhesion, thus orchestrating an immunosuppressive niche in HCC. Intervention with GB1107 disrupted MCTC formation, attenuating the immunosuppressive milieu and potentiating anti-tumor immunity.

Combined therapy of anti-PD-1 antibody and GB1107 significantly inhibited the growth and metastasis of MCTC⁺ HCC *in vivo* by recovering T cell intratumoral infiltration

To assess the therapeutic efficacy of a combined regimen of anti-PD-1 antibody with the Mac-2 antagonist GB1107 on MCTC⁺ HCC, we created two mouse models implanted with Hepa1-6^{M2BPhi} cells. Monitoring revealed that the MCTC was established by day 14 and rapidly increased at day 21 after subcutaneous implantation. Two experimental protocols were tested: one where the anti-PD-1 antibody was administered prior to MCTC formation and another where treatment was initiated after MCTC establishment (Figure 7A). Our findings indicated that administering the anti-PD-1 antibody post-MCTC formation had minimal impact on tumor growth or metastasis. Conversely, early intervention with the anti-PD-1 antibody resulted in a considerable decrease in primary tumor size and lung metastatic nodules (Figures 7B and 7C). mIF staining of tumor tissues showed that CD8⁺ T cells were predominantly localized at the periphery of the MCTC and excluded from the tumor core in control mice. Pre-MCTC formation treatment with the anti-PD-1 antibody substantially increased CD8⁺ T cell infiltration into the tumor nests. Notably, the combination therapy of anti-PD-1 antibody and GB1107 not only significantly impeded MCTC formation but also recovered T cell intratumoral infiltration and overcame local immune deprivation (Figure 7D). Thus, the synergistic effect of anti-PD-1 antibody and Mac-2 antagonist GB1107 markedly attenuated HCC progression and metastasis, highlighting a promising therapeutic strategy for HCC treatment.

DISCUSSION

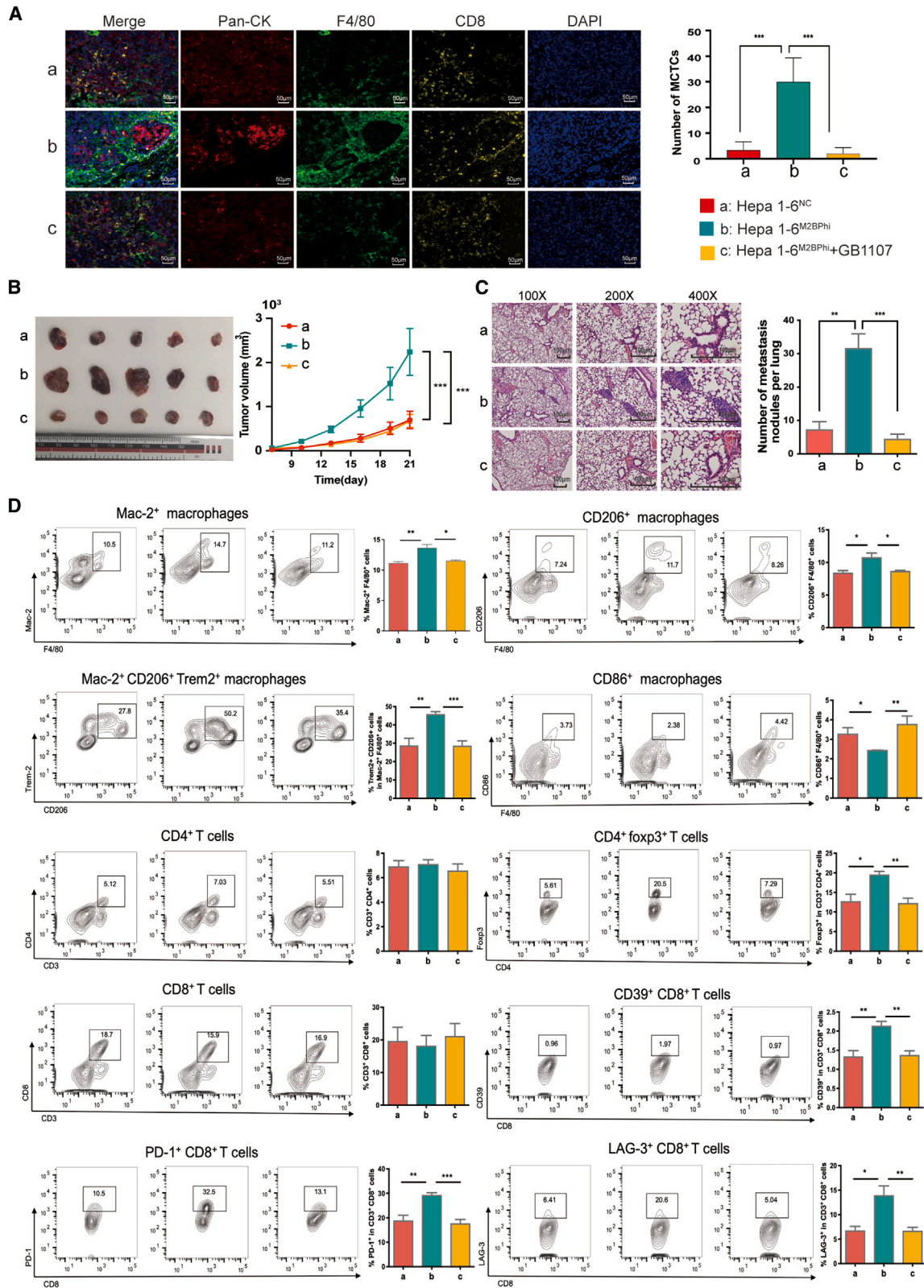
In our study, we have illuminated the paradoxical landscape of MCTC⁺ HCC, where active immune signaling coexists with profound resistance to ICI. The intricate spatial architecture of MCTCs, with cytotoxic T cells relegated to the periphery, impedes their direct anti-tumoral assault. This physical segregation is underpinned by a cadre of M2-like macrophages, particularly the Trem2⁺ subset, that orchestrate an immunosuppressive milieu despite the heightened inflammatory state. The Mac-2⁺ macrophages, driven by tumor-secreted M2BP, further entrench this segregation, contributing to the formation of a robust immunosuppressive barricade that the extracellular matrix (ECM) compounds. This milieu is rendered even more inhospitable by Tregs and an upsurge of T cell exhaustion markers, a reflection of the adaptive immune resistance. Collectively, these elements coalesce to a TME that is immunologically active yet functionally restrained, offering a stark illustration of the complexity of immune evasion in HCC. Consequently, we delve into the immunological quagmire presented by MCTCs in HCC, dissecting the enigmatic dichotomy between apparent immunological activation and concurrent immunotherapy resistance.

Transcriptional profiles of bulk tumors or single-cell sequencing has been used to reveal immune cell clustering and distinct molecular characteristics.^{21,22} However, these could not reflect differences in spatial distribution of immune cells. Leveraging mIF and digital spatial profiling, we have unearthed macrophage heterogeneity and the predictive value of MCTCs in forecasting poor prognosis and resistance to ICI therapy in HCC. Our findings revealed that MCTCs represented structured entities, orchestrated by M2BP-dependent adhesion—a phenomenon further delineated through mIF staining and deep learning AI technology. Further analysis of the TME in MCTC⁺ tissues revealed significant activation of the JAK/STAT and nuclear factor κ B pathways, driving the production of inflammatory mediators that are pivotal for immune cell recruitment and activation within the tumor milieu,²³ thus enriching the “inflammatory response” and chemotaxis pathways. Gene expression profiling of 64 HCC samples from TJMUCH cohort III revealed that most MCTC⁺ issues fell into the immune class defined by Sia et al.,²⁴ marked by inflammatory response and cytolytic activity (65.4% in MCTC⁺ HCC vs. 36.8% in MCTC⁻ HCC, $p = 0.025$). However, the clinical analysis paints a contrasting picture revealing that these hot tumors often exhibit resistance to immunotherapy. Immunofluorescent analysis has shown active immune cells sequestered by CD68⁺ TAMs at the MCTC periphery, while the tumor core is notably lacking in cytotoxic T cell presence. Our research underscores the significance of immune cell spatial distribution, propelling the field toward dynamic spatial visualization of immune cell localization—a key determinant in the effectiveness of immune responses in HCC.

(E) A migration assay was performed to quantify the number of macrophages that migrated when cocultured with tumor cells treated as described above at 24 h. Data are represented as mean \pm SD ($n = 3$ independent experiments).

(F) Adhesion assays presenting the number of macrophages adhering to the tumor cells treated as described above at 24 h. Data are represented as mean \pm SD ($n = 3$ independent experiments).

* $p < 0.05$, ** $p < 0.01$, and *** $p < 0.001$.



(legend on next page)

TAMs prolific within the TME have been implicated in various facets of HCC progression, including angiogenesis, metastasis, and the orchestration of immune suppression, primarily through their secretome of cytokines, chemokines, growth factors, and matrix metalloproteases.^{25–28} The work of Sattiraju et al. has shed light on how the spatiotemporal distribution of TAMs contributes to the immunosuppressive environment in glioblastoma, marking the migration of TAMs from perivascular regions to areas with scant vasculature in response to the tumor's evolving hypoxic state.²⁹ This highlighted the critical role of TAMs in shaping the immune landscape; however, the characterization of these spatially responsive macrophages has been confined to murine models, with clarity lacking in human tissues. Our study addressed a critical gap in human research, identifying a distinctive presence of Trem2⁺ macrophages within MCTC⁺ HCC tissues accompanied by a notable upregulation of pro-tumorigenic traits such as LA-TAMs, Reg-TAMs, and Angio-TAMs. These findings underscore the pivotal role of TAMs in crafting an immunological “cage” within MCTC formations, effectively impeding T cell infiltration, and fostering a localized immune desertification that ultimately leads to resistance to ICI therapy.

Moreover, our scRNA-seq analysis has identified four distinct macrophage clusters. Cluster 1 was primarily found in MCTC⁻ tissues, marked by a gene expression profile associated with the glucose metabolism pathway, such as PPARGC1A, LEPR, or GOT1, essential for the pro-inflammatory phenotype and anti-tumor responses.^{30,31} Conversely, clusters 2, 3, and 4 were predominantly found in MCTC⁺ tissues. Cluster 2 was characterized by genes such as DOCK2, DOCK8, PREX1, DOCK10, and DOCK11, which regulate the activation of small GTPases, exerting a profound influence on immune cell migration, signal transduction, and functional potency.³² The genetic landscape of cluster 3 extended beyond glucose metabolism, revealing a repertoire of genes, including CYP2A6, SULT2A1, G6PC1, and CYP2C8, which are indicative of a metabolic shift from glycolysis to lipolysis—a reprogramming that potentially steers macrophages toward an immunosuppressive phenotype.^{30,33} Concurrently, cluster 4 exhibited an upsurge in genes integral to angiogenesis, like PTPRB, FLT1, CALCRL, VAV3, HSPG2, EPAS1, and COL4A2 (Figure S6A). This suggested that compared to their counterparts in MCTC⁻ tissues, macrophages in MCTC⁺ tissues exhibited pronounced small GTPase pathway activation, metabolic dysregulation, and angiogenic activity, which might enhance their capacity for immunosuppression and pro-metastatic potential.

Although DCs and mast cells were not explicitly delineated in the t-SNE plots, our transcriptional analysis using specific markers for DCs (CLEC9A, FLT3, XCR1) and the mast cell

marker KIT revealed that these cell types were mainly interspersed within the B cell and endothelial cell clusters rather than clustering with the macrophage group. This denoted a sparse distribution of these cell types, as depicted in Figures S6B and S6C. Importantly, this minimal overlap does not impinge upon the robustness of our macrophage-centric analysis, affirming the validity of our core findings on the distinctive behaviors and phenotypes of macrophages within MCTC⁺ HCC tissues.

Our finding revealed that M2BP, secreted by HCC cells, orchestrated macrophage recruitment and enhanced cellular adhesion leading to the formation of MCTC. This is corroborated by scRNA-seq data, which illustrated a disparity in clustering pattern of tumor cells between MCTC⁺ and MCTC⁻ tissues (Figure S6D). Specifically, in MCTC⁺ tissues, there was a significant upregulation of genes associated with cell adhesion, ECM organization, and macrophage migration compared to MCTC⁻ tissues (Figure S6E). Notably, the t-SNE plots highlighted that M2BP was predominantly expressed in MCTC⁺ tumor cells as opposed to MCTC⁻ tumor cells (Figure S6F). Expression analysis further revealed that the M2BP level was significantly elevated in MCTC⁺ tumor cells in comparison to MCTC⁻ tumor cells (Figure S6G), emphasizing the critical role of M2BP in modulating chemotaxis and adhesion within MCTC⁺ HCC.

The ECM, with its intricate composition of fibronectin, collagen, and other adhesion molecules like galectin-1, constitutes a formidable barrier within the TME exerting critical control over T cell trafficking.^{34,35} Concomitantly, TAMs can modulate ECM production through interactions with fibroblasts.³⁶ A recent study discovered that TAMs can be spatially colocalized with fibroblasts, forming an immune barrier that impedes immune cell infiltration in HCC, thereby playing a role in resistance to ICI therapy.³⁷ Our observation indicated that in MCTC⁺ HCC tissues, there was a marked increase in FAP expression within α SMA⁺HepPar-1⁻ fibroblasts compared to MCTC⁻ tissues. However, the majority of FAP⁺ fibroblasts were localized in the tumor cell area within MCTC structures, being separated from the macrophage area at the periphery of MCTC structures (Figure S6H). These results suggested that, different from previous reports,³⁸ the ECM produced by fibroblasts in MCTC might interact with tumor cells. This emphasized that M2BP in tumor cells played a central role in this process by enhancing cell adhesion to the ECM and thus impeding T cell infiltration. Crucially, our research advanced the therapeutic narrative by demonstrating that GB1107, which disrupted M2BP's adhesive hegemony, enhances the efficacy of anti-PD-1 antibody therapy. The synergistic potential of this combinatory approach heralds a promising

Figure 6. Tumor-derived M2BP reinforced the chemotaxis and cell-to-cell adhesion to induce MCTC formation *in vivo*

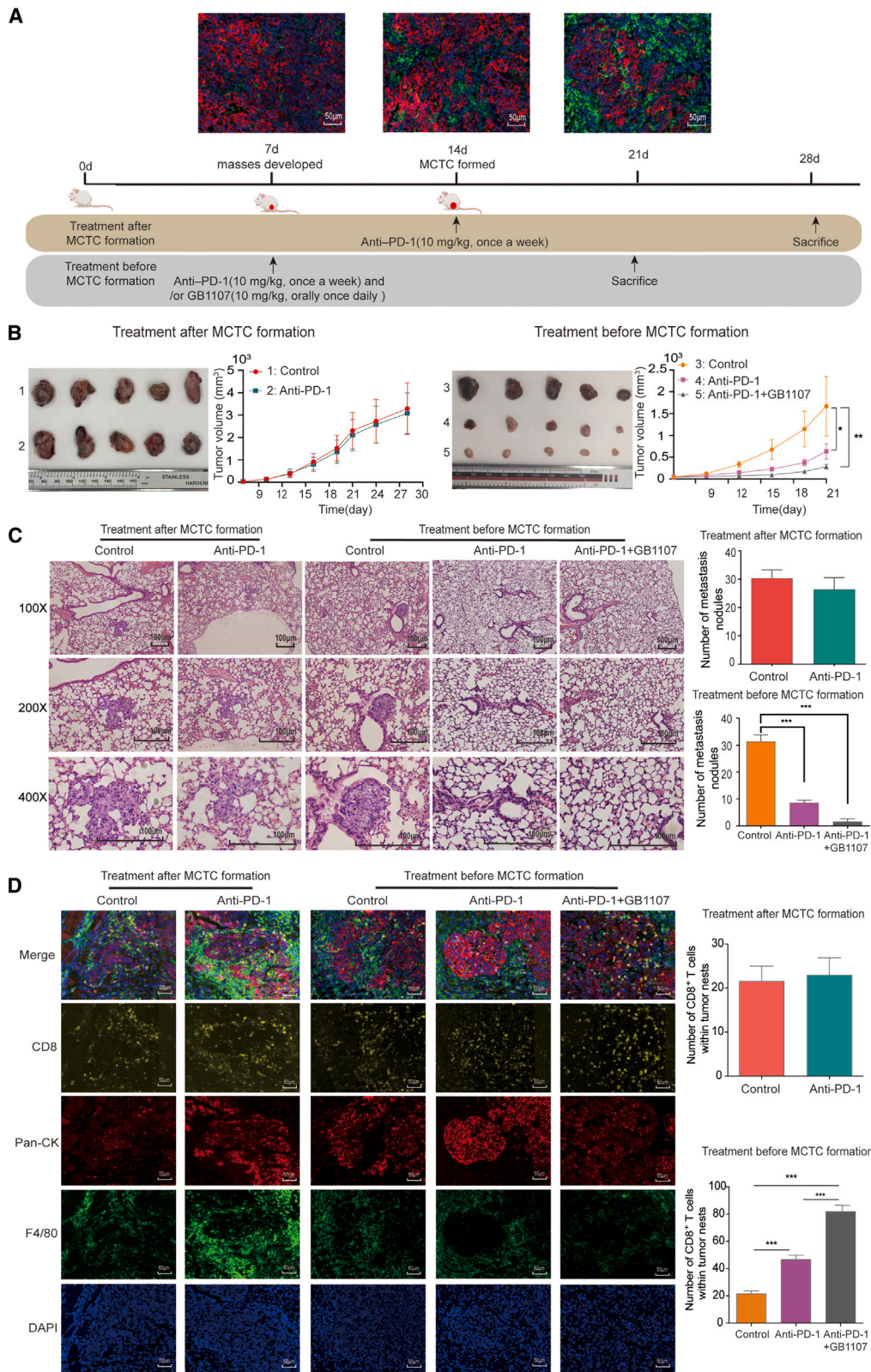
(A) mIF imaging depicting the MCTC structure and distribution of CD8⁺ T cells (left), along with statistical analysis of the MCTC count (right), in C57 mice with subcutaneously implanted Hepa1-6^{NC} and Hepa1-6^{M2BPhⁱ} tumors both with and without GB1107 treatment (scale bars: 50 μ m). *n* = 5 mice per group.

(B) Overview of the tumor mass (left) and tumor growth curves (right) in the subcutaneously implanted tumors of the above groups. *n* = 5 mice per group.

(C) Representative H&E-stained images of pulmonary metastatic nodules (left, scale bars: 100 μ m) and quantitative analysis of metastatic nodules in mice from the above groups. *n* = 5 mice per group.

(D) Quantitative assessment of various cell populations in the subcutaneous tumors of the above groups: Mac-2⁺F4/80⁺ cells, CD206⁺F4/80⁺ cells, CD86⁺F4/80⁺ cells, Trem2⁺CD206⁺Mac-2⁺F4/80⁺ cells, CD3⁺CD8⁺ cells, CD3⁺CD4⁺ cells, CD3⁺CD4⁺Foxp3⁺ cells, CD3⁺CD8⁺PD-1⁺ cells, and CD3⁺CD8⁺LAG-3⁺ cells. *n* = 5 mice per group.

Data are represented as mean \pm SD. **p* < 0.05, ***p* < 0.01, and ****p* < 0.001.



(legend on next page)

avenue for the treatment of MCTC⁺ HCC, underscoring a novel stratagem in the combat against immunotherapy-refractory malignancies.

Contemporary research in HCC has brought to the fore the significance of vessels encapsulating tumor clusters³⁹ and underscored the critical function of TAMs in orchestrating angiogenesis.⁴⁰ Our scRNA-seq analysis has identified significant Angio-TAM features within the macrophages of MCTC⁺ tissues, accompanied by a significantly upregulated angiogenesis pathway. Consequently, we stained for the vascular marker CD31 in MCTC⁺ tissues and observed colocalization with macrophages (Figure S6I), suggesting interactions between macrophages and endothelial cells within MCTC⁺ regions. These insights warrant further investigation into the distinct regulatory mechanisms that govern MCTC formation and their potential as therapeutic targets in HCC.

In our cross-cancer analysis, MCTC emerged as a prevalent structure present in 35.5% of breast cancer and 23.5% of lung squamous carcinoma samples. This manifestation of MCTC correlates with a diminished OS in these cancers, illuminating the prognostic weight of this pattern ($p < 0.05$, Figures S6J and S6K). The association of MCTC with higher AJCC stages in breast cancer, as well as with distal metastasis in lung squamous carcinoma (Tables S7 and S8), underscores the potential of MCTC as a pan-cancer marker for aggressive disease phenotypes. The application of deep-learning-based AI technology for MCTC identification heralds a new era in clinical diagnostics, enhancing accuracy and reducing human error, by providing an efficient and powerful tool for evaluating the prognostic and therapeutic implications of MCTC across various malignancies.

Limitations of the study

A comprehensive analysis of the spatial distribution and interaction among the immune cells in MCTC⁺ tissues is of paramount importance. Our current methodologies, including NanoString DSP and single-cell technologies, do not permit concurrent spatial- and single-cell-level analyses. In future work, we plan to integrate advanced spatial profiling techniques, like single-cell Stereo-seq, to deepen our understanding of the immune landscape in HCC. Additionally, the therapeutic models employed in this study harnessed subcutaneous tumor models for *in vivo* experimentation. However, to truly capture the heterogeneity of the TME, orthotopic tumor models, which more closely mimic the natural setting of the tumor, would be superior. Moreover, our identification of

MCTC structures within breast cancer and lung squamous carcinoma, and their prognostic significance, necessitates further exploration to elucidate the underlying mechanisms. These insights will be crucial for the development of targeted therapies that can disrupt the immune-suppressive milieu fostered by MCTC formations.

STAR★METHODS

Detailed methods are provided in the online version of this paper and include the following:

- KEY RESOURCES TABLE
- RESOURCE AVAILABILITY
 - Lead contact
 - Materials availability
 - Data and code availability
- EXPERIMENTAL MODEL AND STUDY PARTICIPANT DETAILS
 - Patients and specimens
 - Cell culture and generation of the stable cell line
 - Mouse models and treatment protocols
- METHOD DETAILS
 - MIF staining and analysis
 - Classification of spatial patterns of TAMs in HCC
 - Quantitative analysis of immune cells in HCC tissues
 - Deep learning/Development of robustly MCTC
 - Digital spatial profiling of HCC samples
 - Genome-wide expression profiling in HCC
 - ScRNA-seq and bioinformatic analyses
 - RNA extraction and real-time quantitative PCR (RT-qPCR)
 - Live-cell imaging assay
 - Migration assay
 - Cell adhesion assay
 - Immunohistochemical staining
 - Quantification of metastatic nodules in subcutaneous tumors
 - Analysis of immune cell infiltration in subcutaneous tumors
- QUANTIFICATION AND STATISTICAL ANALYSIS

SUPPLEMENTAL INFORMATION

Supplemental information can be found online at <https://doi.org/10.1016/j.xcrm.2024.101505>.

Figure 7. Combined therapy of anti-PD-1 antibody and GB1107 significantly inhibited the growth and metastasis of MCTC⁺ HCC *in vivo* by recovering T cell intratumoral infiltration

(A) C57 mice were sacrificed on days 7, 14, and 21 following subcutaneous tumor implantation to assess the timing of MCTC formation. Two anti-PD-1 therapy models are presented: one post-MCTC formation and one pre-MCTC formation. In the post-MCTC formation model, anti-PD-1 therapy commenced on day 14 after tumor implantation. For the pre-MCTC formation model, anti-PD-1 therapy, either alone or in combination with GB1107, began on day 7 following implantation.

(B) A comprehensive overview of tumor mass and tumor growth curves in the subcutaneous tumors of the two models. $n = 5$ mice per group.

(C) Representative H&E-stained images of pulmonary metastatic nodules (left, scale bars: 100 μm) along with quantification of metastatic nodules (right) in mice from both models. $n = 5$ mice per group.

(D) mIF imaging depicting the MCTC structure and distribution of CD8⁺ T cells (left, scale bars: 50 μm) along with quantification of CD8⁺ T cells within tumor nests (right) in mice from both models. $n = 5$ mice per group.

Data are represented as mean \pm SD. * $p < 0.05$, ** $p < 0.01$, and *** $p < 0.001$.

ACKNOWLEDGMENTS

We thank Dr. Yalei Wang, Bin Feng, and Yong Wang (Department of Pathology, TJMUCH) for giving some pathological help. We thank Dr. Yi Zhao (Chinese Academy of Sciences, Beijing) for help with bioinformatics analysis. This work was supported by the National Natural Science Foundation of China (grant nos. 82002601 and 82203668), the Tianjin Key Medical Discipline (Specialty) Construction Project (TJYXZDXK-009A), and the Project funded by the China Postdoctoral Science Foundation (2023T160481).

AUTHOR CONTRIBUTIONS

Conceptualization and design, J.Y. and X.L.; methodology development, J.N., Y.Y., and H.S.; clinical and pathological sample collection, H.L. and T.S.; image acquisition and analysis, R.Z. and H.W.; pathological analysis, F.Z.; statistical analysis, R.Z.; bioinformatics and other computational analyses, P.L. and G.C.; writing of the manuscript, J.Y. and X.L.; revision of the manuscript, J.N., Y.Y., and H.S. All authors read and approved this manuscript.

DECLARATION OF INTERESTS

The authors declare no competing interests.

Received: May 18, 2023

Revised: November 30, 2023

Accepted: March 19, 2024

Published: April 12, 2024

REFERENCES

- Sung, H., Ferlay, J., Siegel, R.L., Laversanne, M., Soerjomataram, I., Jemal, A., and Bray, F. (2021). Global Cancer Statistics 2020: GLOBOCAN Estimates of Incidence and Mortality Worldwide for 36 Cancers in 185 Countries. *CA: a cancer journal for clinicians* 71, 209–249. <https://doi.org/10.3322/caac.21660>.
- Marisi, G., Petracci, E., Raimondi, F., Faloppi, L., Foschi, F.G., Lauletta, G., Iavarone, M., Canale, M., Valgiusti, M., Neri, L.M., et al. (2019). ANGPT2 and NOS3 Polymorphisms and Clinical Outcome in Advanced Hepatocellular Carcinoma Patients Receiving Sorafenib. *Cancers* 11, 1023. <https://doi.org/10.3390/cancers11071023>.
- Rovesti, G., Orsi, G., Kalliopi, A., Vivaldi, C., Marisi, G., Faloppi, L., Foschi, F.G., Silvestris, N., Pecora, I., Aprile, G., et al. (2019). Impact of Baseline Characteristics on the Overall Survival of HCC Patients Treated with Sorafenib: Ten Years of Experience. *Gastrointestinal Tumors* 6, 92–107. <https://doi.org/10.1159/000502714>.
- Yau, T., Park, J.W., Finn, R.S., Cheng, A.L., Mathurin, P., Edeline, J., Kudo, M., Harding, J.J., Merle, P., Rosmorduc, O., et al. (2022). Nivolumab versus sorafenib in advanced hepatocellular carcinoma (CheckMate 459): a randomised, multicentre, open-label, phase 3 trial. *Lancet. Oncol.* 23, 77–90. [https://doi.org/10.1016/S1470-2045\(21\)00604-5](https://doi.org/10.1016/S1470-2045(21)00604-5).
- El-Khoueiry, A.B., Sangro, B., Yau, T., Crocenzi, T.S., Kudo, M., Hsu, C., Kim, T.Y., Choo, S.P., Trojan, J., Welling, T.H., Rd., et al. (2017). Nivolumab in patients with advanced hepatocellular carcinoma (CheckMate 040): an open-label, non-comparative, phase 1/2 dose escalation and expansion trial. *Lancet* 389, 2492–2502. [https://doi.org/10.1016/S0140-6736\(17\)31046-2](https://doi.org/10.1016/S0140-6736(17)31046-2).
- Saung, M.T., Pelosof, L., Casak, S., Donoghue, M., Lemery, S., Yuan, M., Rodriguez, L., Schotland, P., Chuk, M., Davis, G., et al. (2021). FDA Approval Summary: Nivolumab Plus Ipilimumab for the Treatment of Patients with Hepatocellular Carcinoma Previously Treated with Sorafenib. *Oncol.* 26, 797–806. <https://doi.org/10.1002/onco.13819>.
- Finn, R.S., Ryoo, B.Y., Merle, P., Kudo, M., Bouattour, M., Lim, H.Y., Redder, V., Edeline, J., Chao, Y., Ogasawara, S., et al. (2020). Pembrolizumab As Second-Line Therapy in Patients With Advanced Hepatocellular Carcinoma in KEYNOTE-240: A Randomized, Double-Blind, Phase III Trial. *J. Clin. Oncol.* 38, 193–202. <https://doi.org/10.1200/JCO.19.01307>.
- Greten, T.F., Lai, C.W., Li, G., and Staveley-O'Carroll, K.F. (2019). Targeted and Immune-Based Therapies for Hepatocellular Carcinoma. *Gastroenterology* 156, 510–524. <https://doi.org/10.1053/j.gastro.2018.09.051>.
- Genova, C., Dellepiane, C., Carrega, P., Sommariva, S., Ferlazzo, G., Pronzato, P., Gangemi, R., Filaci, G., Coco, S., and Croce, M. (2021). Therapeutic Implications of Tumor Microenvironment in Lung Cancer: Focus on Immune Checkpoint Blockade. *Front. Immunol.* 12, 799455. <https://doi.org/10.3389/fimmu.2021.799455>.
- Ye, Y., Guo, J., Xiao, P., Ning, J., Zhang, R., Liu, P., Yu, W., Xu, L., Zhao, Y., and Yu, J. (2020). Macrophages-induced long noncoding RNA H19 up-regulation triggers and activates the miR-193b/MAPK1 axis and promotes cell aggressiveness in hepatocellular carcinoma. *Cancer Lett.* 469, 310–322. <https://doi.org/10.1016/j.canlet.2019.11.001>.
- Ning, J., Ye, Y., Bu, D., Zhao, G., Song, T., Liu, P., Yu, W., Wang, H., Li, H., Ren, X., et al. (2021). Imbalance of TGF- β 1/BMP-7 pathways induced by M2-polarized macrophages promotes hepatocellular carcinoma aggressiveness. *Mol. Ther.* 29, 2067–2087. <https://doi.org/10.1016/j.ymthe.2021.02.016>.
- Chamseddine, A.N., Assi, T., Mir, O., and Chouaib, S. (2022). Modulating tumor-associated macrophages to enhance the efficacy of immune checkpoint inhibitors: A TAM-paring approach. *Pharmacology & therapeutics* 231, 107986. <https://doi.org/10.1016/j.pharmthera.2021.107986>.
- Arlaukas, S.P., Garris, C.S., Kohler, R.H., Kitaoka, M., Cuccarese, M.F., Yang, K.S., Miller, M.A., Carlson, J.C., Freeman, G.J., Anthony, R.M., et al. (2017). In vivo imaging reveals a tumor-associated macrophage-mediated resistance pathway in anti-PD-1 therapy. *Sci. Transl. Med.* 9, eaa3604. <https://doi.org/10.1126/scitranslmed.aal3604>.
- Fridman, W.H., Zitvogel, L., Sautès-Fridman, C., and Kroemer, G. (2017). The immune contexture in cancer prognosis and treatment. *Nat. Rev. Clin. Oncol.* 14, 717–734. <https://doi.org/10.1038/nrclinonc.2017.101>.
- Mao, X., Xu, J., Wang, W., Liang, C., Hua, J., Liu, J., Zhang, B., Meng, Q., Yu, X., and Shi, S. (2021). Crosstalk between cancer-associated fibroblasts and immune cells in the tumor microenvironment: new findings and future perspectives. *Mol. Cancer* 20, 131. <https://doi.org/10.1186/s12943-021-01428-1>.
- Gaggioli, C., Hooper, S., Hidalgo-Carcedo, C., Grosse, R., Marshall, J.F., Harrington, K., and Sahai, E. (2007). Fibroblast-led collective invasion of carcinoma cells with differing roles for RhoGTPases in leading and following cells. *Nat. Cell Biol.* 9, 1392–1400. <https://doi.org/10.1038/ncb1658>.
- Duda, D.G., Duyverman, A.M., Kohno, M., Snuderl, M., Steller, E.J., Fukumura, D., and Jain, R.K. (2010). Malignant cells facilitate lung metastasis by bringing their own soil. *Proceedings of the National Academy of Sciences of the United States of America* 107, 21677–21682. <https://doi.org/10.1073/pnas.1016234107>.
- Shen, H., Shen, X., Wu, D., Feng, M., Yang, Y., Li, Y., Yang, M., Wang, W., Zhang, Q., Song, F., et al. (2020). An immunomodulatory signature of responsiveness to immune checkpoint blockade therapy. *Clin. Transl. Med.* 10, e238. <https://doi.org/10.1002/ctm2.238>.
- Ma, R.Y., Black, A., and Qian, B.Z. (2022). Macrophage diversity in cancer revisited in the era of single-cell omics. *Trends Immunol.* 43, 546–563. <https://doi.org/10.1016/j.it.2022.04.008>.
- Binnewies, M., Pollack, J.L., Rudolph, J., Dash, S., Abushawish, M., Lee, T., Jahchan, N.S., Canaday, P., Lu, E., Norng, M., et al. (2021). Targeting TREM2 on tumor-associated macrophages enhances immunotherapy. *Cell Rep.* 37, 109844. <https://doi.org/10.1016/j.celrep.2021.109844>.
- Song, G., Shi, Y., Zhang, M., Goswami, S., Afridi, S., Meng, L., Ma, J., Chen, Y., Lin, Y., Zhang, J., et al. (2020). Global immune characterization of HBV/HCV-related hepatocellular carcinoma identifies macrophage and T-cell subsets associated with disease progression. *Cell discovery* 6, 90. <https://doi.org/10.1038/s41421-020-00214-5>.

22. Zhang, Q., He, Y., Luo, N., Patel, S.J., Han, Y., Gao, R., Modak, M., Carotta, S., Haslinger, C., Kind, D., et al. (2019). Landscape and Dynamics of Single Immune Cells in Hepatocellular Carcinoma. *Cell* 179, 829–845.e20. <https://doi.org/10.1016/j.cell.2019.10.003>.
23. Zhao, H., Wu, L., Yan, G., Chen, Y., Zhou, M., Wu, Y., and Li, Y. (2021). Inflammation and tumor progression: signaling pathways and targeted intervention. *Signal Transduct Target Ther* 6, 263. <https://doi.org/10.1038/s41392-021-00658-5>.
24. Sia, D., Jiao, Y., Martinez-Quetglas, I., Kuchuk, O., Villacorta-Martin, C., Castro de Moura, M., Putra, J., Camprecios, G., Bassaganyas, L., Akers, N., et al. (2017). Identification of an Immune-specific Class of Hepatocellular Carcinoma, Based on Molecular Features. *Gastroenterology* 153, 812–826. <https://doi.org/10.1053/j.gastro.2017.06.007>.
25. Bao, D., Zhao, J., Zhou, X., Yang, Q., Chen, Y., Zhu, J., Yuan, P., Yang, J., Qin, T., Wan, S., and Xing, J. (2019). Mitochondrial fission-induced mtDNA stress promotes tumor-associated macrophage infiltration and HCC progression. *Oncogene* 38, 5007–5020. <https://doi.org/10.1038/s41388-019-0772-z>.
26. Li, X., Yao, W., Yuan, Y., Chen, P., Li, B., Li, J., Chu, R., Song, H., Xie, D., Jiang, X., and Wang, H. (2017). Targeting of tumour-infiltrating macrophages via CCL2/CCR2 signalling as a therapeutic strategy against hepatocellular carcinoma. *Gut* 66, 157–167. <https://doi.org/10.1136/gutjnl-2015-310514>.
27. Capece, D., Fischietti, M., Verzella, D., Gaggiano, A., Ciccirelli, G., Tessitore, A., Zazzeroni, F., and Alesse, E. (2013). The inflammatory microenvironment in hepatocellular carcinoma: a pivotal role for tumor-associated macrophages. *BioMed Res. Int.* 2013, 187204. <https://doi.org/10.1155/2013/187204>.
28. Hernandez-Gea, V., Toffanin, S., Friedman, S.L., and Llovet, J.M. (2013). Role of the microenvironment in the pathogenesis and treatment of hepatocellular carcinoma. *Gastroenterology* 144, 512–527. <https://doi.org/10.1053/j.gastro.2013.01.002>.
29. Sattiraju, A., Kang, S., Giotti, B., Chen, Z., Marallano, V.J., Brusco, C., Ramakrishnan, A., Shen, L., Tsankov, A.M., Hambardzumyan, D., et al. (2023). Hypoxic niches attract and sequester tumor-associated macrophages and cytotoxic T cells and reprogram them for immunosuppression. *Immunity* 56, 1825–1843.e6. <https://doi.org/10.1016/j.immuni.2023.06.017>.
30. Wculek, S.K., Dunphy, G., Heras-Murillo, I., Mastrangelo, A., and Sancho, D. (2022). Metabolism of tissue macrophages in homeostasis and pathology. *Cell. Mol. Immunol.* 19, 384–408. <https://doi.org/10.1038/s41423-021-00791-9>.
31. Viola, A., Munari, F., Sánchez-Rodríguez, R., Scolaro, T., and Castegna, A. (2019). The Metabolic Signature of Macrophage Responses. *Front. Immunol.* 10, 1462. <https://doi.org/10.3389/fimmu.2019.01462>.
32. Yin, G., Huang, J., Petela, J., Jiang, H., Zhang, Y., Gong, S., Wu, J., Liu, B., Shi, J., and Gao, Y. (2023). Targeting small GTPases: emerging grasps on previously untamable targets, pioneered by KRAS. *Signal Transduct. Target. Ther.* 8, 212. <https://doi.org/10.1038/s41392-023-01441-4>.
33. Qiao, X., Hu, Z., Xiong, F., Yang, Y., Peng, C., Wang, D., and Li, X. (2023). Lipid metabolism reprogramming in tumor-associated macrophages and implications for therapy. *Lipids Health Dis.* 22, 45. <https://doi.org/10.1186/s12944-023-01807-1>.
34. Salmon, H., Franciszkiewicz, K., Damotte, D., Dieu-Nosjean, M.C., Validire, P., Trautmann, A., Mami-Chouaib, F., and Donnadieu, E. (2012). Matrix architecture defines the preferential localization and migration of T cells into the stroma of human lung tumors. *J. Clin. Invest.* 122, 899–910. <https://doi.org/10.1172/jci45817>.
35. Bu, X., Mahoney, K.M., and Freeman, G.J. (2016). Learning from PD-1 Resistance: New Combination Strategies. *Trends Mol. Med.* 22, 448–451. <https://doi.org/10.1016/j.molmed.2016.04.008>.
36. Witherell, C.E., Sao, K., Brisson, B.K., Han, B., Volk, S.W., Petrie, R.J., Han, L., and Spiller, K.L. (2021). Regulation of extracellular matrix assembly and structure by hybrid M1/M2 macrophages. *Biomaterials* 269, 120667. <https://doi.org/10.1016/j.biomaterials.2021.120667>.
37. Liu, Y., Xun, Z., Ma, K., Liang, S., Li, X., Zhou, S., Sun, L., Liu, Y., Du, Y., Guo, X., et al. (2023). Identification of a tumour immune barrier in the HCC microenvironment that determines the efficacy of immunotherapy. *J. Hepatol.* 78, 770–782. <https://doi.org/10.1016/j.jhep.2023.01.011>.
38. Buechler, M.B., Fu, W., and Turley, S.J. (2021). Fibroblast-macrophage reciprocal interactions in health, fibrosis, and cancer. *Immunity* 54, 903–915. <https://doi.org/10.1016/j.immuni.2021.04.021>.
39. Renne, S.L., Woo, H.Y., Allegra, S., Rudini, N., Yano, H., Donadon, M., Viganò, L., Akiba, J., Lee, H.S., Rhee, H., et al. (2020). Vessels Encapsulating Tumor Clusters (VETC) Is a Powerful Predictor of Aggressive Hepatocellular Carcinoma. *Hepatology (Baltimore, Md)* 71, 183–195. <https://doi.org/10.1002/hep.30814>.
40. Ran, S., and Montgomery, K.E. (2012). Macrophage-mediated lymphangiogenesis: the emerging role of macrophages as lymphatic endothelial progenitors. *Cancers* 4, 618–657. <https://doi.org/10.3390/cancers4030618>.
41. Hoefsmit, E.P., Rozeman, E.A., Van, T.M., Dimitriadis, P., Krijgsman, O., Conway, J.W., Pires da Silva, I., van der Wal, J.E., Ketelaars, S.L.C., Bresser, K., et al. (2020). Comprehensive analysis of cutaneous and uveal melanoma liver metastases. *Journal for Immunotherapy of Cancer* 8. <https://doi.org/10.1136/jitc-2020-001501>.
42. Hou, X., Shi, X., Zhang, W., Li, D., Hu, L., Yang, J., Zhao, J., Wei, S., Wei, X., Ruan, X., et al. (2021). LDHA induces EMT gene transcription and regulates autophagy to promote the metastasis and tumorigenesis of papillary thyroid carcinoma. *Cell Death Dis.* 12, 347. <https://doi.org/10.1038/s41419-021-03641-8>.
43. Xiao, P., Long, X., Zhang, L., Ye, Y., Guo, J., Liu, P., Zhang, R., Ning, J., Yu, W., Wei, F., and Yu, J. (2018). Neurotensin/IL-8 pathway orchestrates local inflammatory response and tumor invasion by inducing M2 polarization of Tumor-Associated macrophages and epithelial-mesenchymal transition of hepatocellular carcinoma cells. *Oncolimmunology* 7, e1440166. <https://doi.org/10.1080/2162402x.2018.1440166>.
44. Vuong, L., Kouverianou, E., Rooney, C.M., McHugh, B.J., Howie, S.E.M., Gregory, C.D., Forbes, S.J., Henderson, N.C., Zetterberg, F.R., Nilsson, U.J., et al. (2019). An Orally Active Galectin-3 Antagonist Inhibits Lung Adenocarcinoma Growth and Augments Response to PD-L1 Blockade. *Cancer Res.* 79, 1480–1492. <https://doi.org/10.1158/0008-5472.can-18-2244>.
45. Triplett, T.A., Garrison, K.C., Marshall, N., Donkor, M., Blazeck, J., Lamb, C., Qerqez, A., Dekker, J.D., Tanno, Y., Lu, W.C., et al. (2018). Reversal of indoleamine 2,3-dioxygenase-mediated cancer immune suppression by systemic kynurenine depletion with a therapeutic enzyme. *Nat. Biotechnol.* 36, 758–764. <https://doi.org/10.1038/nbt.4180>.
46. Ning, J., Ye, Y., Bu, D., Zhao, G., Song, T., Liu, P., Yu, W., Wang, H., Li, H., Ren, X., et al. (2021). Imbalance of TGF- β 1/BMP-7 pathways induced by M2-polarized macrophages promotes hepatocellular carcinoma aggressiveness. *Mol. Ther.* <https://doi.org/10.1016/j.yjth.2021.02.016>.
47. Yan, C., Huang, H., Zheng, Z., Ma, X., Zhao, G., Zhang, T., Chen, X., Cao, F., Wei, H., Dong, J., et al. (2023). Spatial distribution of tumor-infiltrating T cells indicated immune response status under chemoradiotherapy plus PD-1 blockade in esophageal cancer. *Front. Immunol.* 14, 1138054. <https://doi.org/10.3389/fimmu.2023.1138054>.
48. Huang, G., Liu, Z., van der Maaten, L., and Weinberger, K.Q. (2016). *Densely Connected Convolutional Networks*.
49. Zhou, D., Tian, F., Tian, X., Sun, L., Huang, X., Zhao, F., Zhou, N., Chen, Z., Zhang, Q., Yang, M., et al. (2020). Diagnostic evaluation of a deep learning model for optical diagnosis of colorectal cancer. *Nat. Commun.* 11, 2961. <https://doi.org/10.1038/s41467-020-16777-6>.
50. Meng, L., Elzen, S.V.D., Pezzotti, N., and Vilanova, A. (2023). Class-constrained t-SNE: Combining Data Features and Class Probabilities. *IEEE Trans. Vis. Comput. Graph.*, 1–11. <https://doi.org/10.1109/tvcg.2023.3326600>.
51. Merritt, C.R., Ong, G.T., Church, S.E., Barker, K., Danaher, P., Geiss, G., Hoang, M., Jung, J., Liang, Y., McKay-Fleisch, J., et al. (2020). Multiplex digital spatial profiling of proteins and RNA in fixed tissue. *Nat. Biotechnol.* 38, 586–599. <https://doi.org/10.1038/s41587-020-0472-9>.

52. Chen, Z.P., Wang, S., Zhao, X., Fang, W., Wang, Z., Ye, H., Wang, M.J., Ke, L., Huang, T., Lv, P., et al. (2023). Lipid-accumulated reactive astrocytes promote disease progression in epilepsy. *Nat. Neurosci.* 26, 542–554. <https://doi.org/10.1038/s41593-023-01288-6>.
53. Korsunsky, I., Millard, N., Fan, J., Slowikowski, K., Zhang, F., Wei, K., Baiglaenko, Y., Brenner, M., Loh, P.R., and Raychaudhuri, S. (2019). Fast, sensitive and accurate integration of single-cell data with Harmony. *Nat. Methods* 16, 1289–1296. <https://doi.org/10.1038/s41592-019-0619-0>.
54. Traag, V.A., Waltman, L., and van Eck, N.J. (2019). From Louvain to Leiden: guaranteeing well-connected communities. *Sci. Rep.* 9, 5233. <https://doi.org/10.1038/s41598-019-41695-z>.
55. He, J., Zhou, M., Yin, J., Wan, J., Chu, J., Jia, J., Sheng, J., Wang, C., Yin, H., and He, F. (2021). METTL3 restrains papillary thyroid cancer progression via m(6)A/c-Rel/IL-8-mediated neutrophil infiltration. *Mol. Ther.* 29, 1821–1837. <https://doi.org/10.1016/j.ymthe.2021.01.019>.
56. Ning, J., Hou, X., Hao, J., Zhang, W., Shi, Y., Huang, Y., Ruan, X., Zheng, X., and Gao, M. (2023). METTL3 inhibition induced by M2 macrophage-derived extracellular vesicles drives anti-PD-1 therapy resistance via M6A-CD70-mediated immune suppression in thyroid cancer. *Cell Death Differ.* 30, 2265–2279. <https://doi.org/10.1038/s41418-023-01217-x>.
57. Li, R., Huang, Y., and Lin, J. (2020). Distinct effects of general anesthetics on lung metastasis mediated by IL-6/JAK/STAT3 pathway in mouse models. *Nat. Commun.* 11, 642. <https://doi.org/10.1038/s41467-019-14065-6>.

STAR★METHODS

KEY RESOURCES TABLE

REAGENT or RESOURCE	SOURCE	IDENTIFIER
Antibodies		
Hepatocyte Specific Antigen Antibody	Santa Cruz	Cat# sc-58693; RRID:AB_781327
CD68 Monoclonal Antibody (KP1)	Invitrogen	Cat# 14-0688-82; RRID:AB_11151139
Recombinant Anti-CD8 alpha antibody	Abcam	Cat# ab237709; RRID:AB_2892677
Anti-Human FAP Antibody	Invitrogen	Cat# BMS168; RRID:AB_187837
Recombinant Anti-CD31 antibody	Abcam	Cat# ab76533; RRID:AB_1523298
TREM2 Polyclonal Antibody	Invitrogen	Cat# PA5-18763; RRID:AB_10984816
Recombinant Anti-FOXP3 antibody	Abcam	Cat# ab215206; RRID:AB_2860568
Recombinant Anti-CD39 antibody	Abcam	Cat# ab223842; RRID:AB_2889212
Recombinant Anti-pan Cytokeratin antibody	Abcam	Cat# ab7753; RRID:AB_306047
Monoclonal Anti-Actin, α -Smooth Muscle	Sigma-Aldrich	Cat# A2547; RRID:AB_476701
Anti-CD163 antibody	Abcam	Cat# ab182422; RRID:AB_2753196
Anti-LGALS3BP antibody	Abcam	Cat# ab217760; RRID: AB_3075495
F4/80 (D2S9R) XP [®] Rabbit mAb	Cell Signaling Technology	Cat# 70076; RRID:AB_2799771
CD8 α (D4W2Z) XP [®] Rabbit mAb	Cell Signaling Technology	Cat# 98941; RRID:AB_2813554
PE/Dazzle [™] 594 anti-mouse F4/80	Biolegend	Cat# 123146; RRID:AB_2564133
PE anti-mouse/human Mac-2	Biolegend	Cat# 125405; RRID:AB_2136764
PE/Cyanine7 anti-mouse CD86	Biolegend	Cat# 105013; RRID:AB_439783
APC anti-mouse CD206	Biolegend	Cat# 141707; RRID:AB_10900231
FITC anti-mouse TREM2	Invitrogen	Cat# MA5-28223; RRID:AB_2745193
PerCP/Cyanine5.5 anti-mouse CD3 ϵ	Biolegend	Cat# 155616; RRID:AB_2819909
FITC anti-mouse CD4	Biolegend	Cat# 116003; RRID:AB_313688
APC/Cyanine7 anti-mouse CD8a	Biolegend	Cat# 100713; RRID:AB_312753
PE anti-mouse FOXP3	Biolegend	Cat# 126403; RRID:AB_1089118
Brilliant Violet 421 [™] anti-mouse PD-1	Biolegend	Cat# 135217; RRID:AB_2562568
PE/Cyanine7 anti-mouse CD39	Biolegend	Cat# 143805; RRID:AB_2563393
APC anti-mouse LAG-3	Biolegend	Cat# 125209; RRID:AB_10639727
Bacterial and virus strains		
pHBLV-U6-MCS-EF1-ZsGreen-T2A-Luc	Hanbio Biotechnology	N/A
pHBLV-CMV-MCS-EF1-ZsGreen-T2A-luc	Hanbio Biotechnology	N/A
Biological samples		
Human HCC tissues	Tianjin Medical University Cancer Institute and Hospital	N/A
Human HCC tissues	Xinchao Biotechnology	N/A
Human HCC tissues	Yaxiang Biotechnology	N/A
Human breast cancer tissues	Tianjin Medical University Cancer Institute and Hospital	N/A
Human lung squamous carcinoma tissues	Tianjin Medical University Cancer Institute and Hospital	N/A
Chemicals, peptides, and recombinant proteins		
ProLong Gold Antifade Reagent	Invitrogen	Cat# P36930
Recombinant Human IL-8 (CXCL8)	PeptoTech	Cat# 200-08

(Continued on next page)

Continued		
REAGENT or RESOURCE	SOURCE	IDENTIFIER
GB1107	MedChemExpress	Cat# HY-114409
Cell Tracker™ Red CMTPX Dye	Invitrogen	Cat# C34552
InVivoMAb anti-mouse PD-1	BioXCell	Cat# RMP1-14
Collagenase IV	GlpBio	Cat# GC19591
DNase I	GlpBio	Cat# GC19804
Zombie Aqua™ Fixable Viability Kit	Biolegend	Cat# 423101
Critical commercial assays		
Opal 4-Color Manual IHC Kit	AKOYA Biosciences	Cat# NEL810001KT
Opal 7-Color Manual IHC Kit	AKOYA Biosciences	NEL871001KT
Deposited data		
scRNA-seq	This paper	GEO: GSE248907
Experimental models: Cell lines		
THP-1	ATCC	TIB-202; RRID:CVCL_0006
MHCC97L	Cellcook Biotech Co.	N/A; RRID:CVCL_4973
MHCC97H	Cellcook Biotech Co.	N/A; RRID:CVCL_4972
Hepa1-6	ATCC	CRL-1830; RRID:CVCL_0327
Experimental models: Organisms/strains		
Mouse: C57BL/6	Jiangsu GemPharmatech	N/A
Oligonucleotides		
Primer Human M2BP Forward 5'-CAATGGTACTTCTACTCCCGAA-3'	This paper	N/A
Primer Human M2BP Reverse 5'-GAACTGTAGGCAGAGCTTCTC-3'	This paper	N/A
Primer Mouse M2BP Forward 5'-CTTCTCGTGACCTCTAACGAG-3'	This paper	N/A
Primer Mouse M2BP Reverse 5'-CTGTTCTCATAGCCAATTGTCTG -3'	This paper	N/A
Human ACTB Endogenous Reference Genes Primers	Sangon Biotech	B661102
Mouse ACTB Endogenous Reference Genes Primers	Sangon Biotech	B661302
Software and algorithms		
StrataQuest Image Analysis software	TissueGnostics	https://tissuegnostics.com/products/contextual-image-analysis/strataquest-apps
Cell Ranger software (v6.0.2)	10X Genomics	https://support.10xgenomics.com/singlecell-gene-expression/software
Scanpy (version 1.9.3)	https://pypi.org/project/scanpy/	https://pypi.org/project/scanpy/
Harmony	Korsunsky et al. ⁴¹	https://github.com/immunogenomics/harmony
Leiden algorithm	Traag et al. ⁴²	N/A
SPSS 16.0	https://www.ibm.com/products/spss-statistics	https://www.ibm.com/products/spss-statistics
GraphPad Prism 8	GraphPad	https://www.graphpad.com/features
FlowJo v10.9	FlowJo LLC	https://www.flowjo.com
MedCalc software	https://www.medcalc.org/	https://www.medcalc.org/

RESOURCE AVAILABILITY

Lead contact

Further information and requests regarding this manuscript should be directed to and will be fulfilled by the lead contact Jinpu Yu (jyu@tmu.edu.cn).

Materials availability

The authors declare that all the results supporting the findings of this study are available within the paper and its supplemental materials.

Data and code availability

- The single-cell RNA sequencing dataset in this study has been deposited to the NCBI Gene Expression Omnibus database, and the accession number is GEO: GSE248907.
- This paper does not report original code.
- Any additional information required to reanalyze the data reported in this work paper is available from the [lead contact](#) upon request.

EXPERIMENTAL MODEL AND STUDY PARTICIPANT DETAILS

Patients and specimens

This study encompassed 600 cases of HCC. Specifically, 345 patients who underwent curative resection at the Department of Hepatology, Tianjin Medical University Cancer Institute and Hospital, between November 2007 and November 2020, were categorized into the TJMUCH cohort. This cohort was further divided into four groups based on the period of surgery (Cohort I: n = 133, Cohort II: n = 120, Cohort III: n = 64, Cohort IV: n = 28). To bolster the validity of our findings, we incorporated two independent external cohorts derived from commercial tissue microarrays. The validation set encompassed 175 HCC samples from three medical centers, supplied by Xinchao Biotechnology in Shanghai, along with 80 HCC samples from two medical centers provided by Yaxiang Biotechnology in Changsha. These samples, sourced from diverse medical centers, offer a comprehensive external validation for our study. Prior informed consent was secured from all participating patients. The prevalence of MCTC was examined in a total of 600 paraffin-embedded HCC tissues using multispectral imaging from multiplex immunofluorescence (mIF). While the TJMUCH cohort was assessed using whole-section samples for mIF analysis, the external cohorts were evaluated through tissue microarrays. The prognostic relevance of MCTC was determined in 572 HCC cases, excluding the 28 from TJMUCH Cohort IV. The potential of MCTC to predict the clinical response to ICI therapy was specifically examined in the 28 HCC patients from TJMUCH Cohort IV. To elucidate the molecular mechanisms underlying MCTC formation and ICI resistance, analyses were conducted using NanoString GeoMx digital spatial profiling on 7 HCC samples, single-cell RNA sequencing (scRNA-seq) on 6 samples, and Affymetrix GeneChip whole-genome expression profiling on 64 samples. This investigation received the endorsement of the Ethics Committee at Tianjin Medical University Cancer Institute and Hospital.

Cell culture and generation of the stable cell line

The human leukemia monocytic cell line THP-1, as well as the HCC cell lines MHCC97L and MHCC97H, and the murine HCC cell line Hepa1-6, were all procured from Guangzhou Cellcook Biotech Co. (Guangzhou, P.R. China). The THP-1 cell line was cultivated in RPMI 1640 medium produced by Gibco, enriched with 10% fetal bovine serum (FBS) sourced from Biological Industries in Israel. Meanwhile, the MHCC97L, MHCC97H, and Hepa1-6 cell lines were cultured in Dulbecco's Modified Eagle Medium (DMEM), also from Gibco, with an addition of 10% FBS. All cells were kept at a consistent temperature of 37°C, in a humidified chamber with 5% carbon dioxide. The identity of each cell line was confirmed via short tandem repeat (STR) profiling. To induce the formation of non-adherent macrophages, THP-1 cells were treated with human interleukin-8 (IL-8) (PeproTech, 200-08), at a concentration of 5 ng/mL for 72 h, replicating previously reported protocols.⁴³

Cells were transduced with lentiviral vectors carrying shRNA plasmids or vectors bearing M2BP cDNA constructs to create stable cell lines with either reduced or augmented expression of M2BP. The specific shRNA sequence targeting M2BP was designed as GATCCGGAAGTCAACTGGTCTATTCAAGAGATAGACCAGTT-GTGACTTCCTTTTTTG.

Mouse models and treatment protocols

The animal model was established in line with methodologies reported in a prior study. Hepa1-6 cells (1×10^6) suspended in 100 μ L of PBS were subcutaneously inoculated into the right posterior flank of male C57 mice (4–5 weeks, acquired from Jiangsu GemPharmatech). Upon tumor formation, the GB1107 (10 mg/kg, MedChemExpress, Cat# HY-114409)⁴⁴ was administered orally daily over a two-week period. For the anti-PD-1 therapy model post-MCTC formation, the anti-PD-1 antibody (10 mg/kg, BioXCell, Cat# RMP1-14)⁴⁵ was delivered via intraperitoneal injection weekly for two weeks, commencing on day 14 post-tumor implantation. At 28 days after cell implantation, mice were euthanized for analysis. In the pre-MCTC formation model with anti-PD-1 therapy, treatment with anti-PD-1, alone or in combination with GB1107, was initiated on day 7 post-implantation, and mice were euthanized after 21 days. Tumor dimensions—length (L) and width (W)—were ascertained using calipers, and tumor volume (V) was calculated with the formula: $V = \pi L \times W^2 / 6$. Tumors were bisected; one-half was allocated for flow cytometry, the other for mIF staining. Lung tissue sections were subjected to hematoxylin and eosin (HE) staining to evaluate metastatic dissemination. This investigation received the endorsement of the Ethics Committee at Tianjin Medical University Cancer Institute and Hospital. All animal-related procedures were meticulously aligned with the International Guide for the Care and Use of Laboratory Animals, with stringent measures taken to reduce the number of animals used and alleviate their distress.

METHOD DETAILS

MIF staining and analysis

MIF staining was conducted according to the protocol outlined in our previous publication.⁴⁶ Concisely, tissue slides were first subjected to heat-induced epitope retrieval, followed by deparaffinization in xylene and a graded series of alcohols for rehydration. Subsequent to antigen retrieval and blocking steps, primary antibodies were applied to the slides and incubated at 4°C overnight. Detection involved the use of Opal polymer horseradish peroxidase (HRP) as the secondary antibody. Following thorough washing, slides underwent tyramide signal amplification (TSA) using dyes from the Opal 4 Color Kit (AKOYA Biosciences, Cat# NEL810001KT) and the Opal 7 Color Kit (AKOYA Biosciences, Cat# NEL821001KT). To prepare for the application of additional antibodies, slides were microwaved to remove the initial antibodies, then washed and blocked again. A second set of primary antibodies and 4',6-diamidino-2-phenylindole (DAPI) were subsequently applied. Slides were finally mounted with ProLong Gold Antifade Reagent (Invitrogen, Cat# P36930). The primary antibodies utilized included anti-HepPar-1 (Santa Cruz, Cat# sc-58693), anti-CD68 (Invitrogen, Cat# 14-0688-82), anti-CD163 (Abcam, Cat# ab182422), anti-CD8 (Abcam, Cat# ab237709), anti-CD31 (Abcam, Cat# ab76533), anti-TREM2 (Invitrogen, Cat# PA5-18763), anti-Foxp3 (Abcam, Cat# ab215206), anti-CD39 (Abcam, Cat# ab223842), anti-FAP (Invitrogen, Cat# BMS168), anti- α SMA (Sigma-Aldrich, Cat# A2547), and anti-Pan Cytokeratin (Abcam, Cat# ab7753).

Classification of spatial patterns of TAMs in HCC

In HCC tissues, HepPar-1 positive cells were identified as HCC cells, and CD68 positivity marked TAMs. We utilized a Zeiss microscope equipped with a 10x objective lens for whole slide scanning, which facilitated the examination of tumor cell structural patterns and TAM distribution within tumor nests. Independently reviewed by two pathologists, tumor cell structures were characterized as either aggregated tumor clusters or compactly arranged tumor cells. TAMs distribution was categorized as either dispersed among tumor cells or localized at tumor cluster edges.

From the whole slide images, five representative fields displaying these characteristics were selected for detailed analysis using a TissueGnostics multispectral microscope with a 20x objective lens. The StrataQuest Image Analysis software was employed to precisely demarcate the tumor conglomerate regions. This tool enabled us to accurately quantify the number of TAMs within a 10 μ m perimeter extending from the region's periphery, referred to as TAMs-10 μ m. Additionally, it facilitated the comprehensive enumeration of the overall TAMs population, denoted as total-TAMs.

Subsequently, we adopted a quantitative stratification approach to evaluate TAMs distribution within tissue samples. For tissues wherein TAMs are dispersed among tumor cells, a ratio exceeding 100 (median value) upon division of total TAMs by five denotes a high density of TAMs, referred to as TAMs-HD (High Dispersed). Conversely, a ratio of 100 or less is indicative of a low density of dispersed TAMs, termed TAMs-LD (Low Dispersed). In cases where TAMs are preferentially localized at the edges of tumor clusters, a different metric is applied. Here, a count of TAMs-10 μ m divided by five that surpasses the median of 50 classifies the sample as having a high amount of TAMs at the tumor periphery, designated as TAMs-HS (High Surrounding). If the count is 50 or fewer, it signifies a low amount of peripherally localized TAMs, denoted as TAMs-LS (Low Surrounding).

Finally, we employed a logistic regression model to establish a model based on these four categories, with the logistic regression formulae delineating the spatial pattern signatures for these categories being as follows:

TAMs-LD = $-1.918 * (\text{total-TAMs}) - 1.618 * (\text{tumor cluster status}) - 0.189 * (\text{TAMs-10}\mu\text{m})$; TAMs-LS = $1.658 * (\text{total-TAMs}) - 1.378 * (\text{tumor cluster status}) - 0.415 * (\text{TAMs-10}\mu\text{m})$; TAMs-HD = $-1.337 * (\text{total-TAMs}) + 1.798 * (\text{tumor cluster status}) - 1.004 * (\text{TAMs-10}\mu\text{m})$; TAMs-HS = $1.597 * (\text{total-TAMs}) + 1.197 * (\text{tumor cluster status}) + 1.609 * (\text{TAMs-10}\mu\text{m})$.

Quantitative analysis of immune cells in HCC tissues

Following our established imaging protocol, five representative fields from each tissue specimen were captured using a 20x objective lens. The spectral library provided by StrataQuest Image Analysis software facilitated the unmixing of channels, enabling precise segmentation and scoring of the tissues and cells. Through this software, we quantified the populations of CD8⁺ T cells, Foxp3⁺ cells, CD39⁺ cells, and Trem2⁺CD68⁺ dual-positive macrophages within the captured fields. Aggregation of the total cell counts for each marker across the fields yielded a mean frequency, derived by normalizing the aggregate cell count to the number of fields analyzed (n = 5).

To assess the distribution of CD8⁺ T cells, we first delineated the tumor conglomerate regions using StrataQuest Image Analysis software. CD8⁺ T cells located outside these regions were classified as "excluded". We then conducted a precise enumeration of these excluded CD8⁺ T cells.

To calculate the average distances between CD68⁺ macrophages, CD68⁺CD163⁺ M2 polarized macrophages, and tumor-infiltrating T cells, including CD8⁺ and Foxp3⁺ subsets, we followed the methodology of Yan et al.⁴⁷ Utilizing StrataQuest Image Analysis software, we assessed the proximity of each CD8⁺ T cell to the nearest CD68⁺ macrophages or CD68⁺CD163⁺ M2 polarized macrophages. An analogous approach was applied to measure the distances from each Foxp3⁺ T cell to the closest CD68⁺ macrophages or CD68⁺CD163⁺ M2 polarized macrophages. By compiling these individual measurements, we were able to compute an average value, providing a representative mean distance across the cellular landscape.

Deep learning/Development of robustly MCTC

For robust classification of MCTC, we developed a deep convolutional neural network (DCNN) model. This model was trained to classify mIF-stained image pixels into two categories: MCTC-positive or MCTC-negative. The architecture of the model is based on DenseNet with 64 layers (DenseNet-64),⁴⁸ augmented by a densely connected topology that captures and retains abstract features of the input images through a fully connected layer dedicated to image classification. The training dataset comprised 323 MCTC-positive and 25,061 MCTC-negative image patches. We initialized the DCNN model's weights using the pre-trained CRCNet model⁴⁹ and employed the stochastic gradient descent algorithm⁴⁸ for optimization. To enhance the model's robustness and prevent overfitting, we implemented several data augmentation techniques such as random cropping, horizontal and vertical flipping, and the addition of Gaussian blur and noise. The model's discriminative performance was quantified using the Precision-Recall Area Under the Curve (PRAUC), which plots precision against recall to assess the accuracy of MCTC⁺ image identification. PRAUC values were computed using the "sklearn" library in Python (version 0.24.2), providing a comprehensive measure of the model's classification ability. T-distributed stochastic neighborhood embedding (tSNE)⁵⁰ was employed for image embedding feature visualization.

Digital spatial profiling of HCC samples

We utilized the NanoString GeoMx Digital Spatial Profiling (DSP) technology, a highly multiplexed method for spatial profiling of mRNAs and proteins in predefined regions of interest (ROIs) within formalin-fixed paraffin-embedded (FFPE) tissue sections.⁵¹ Multiplexed and spatially resolved profiling analysis on pretreatment FFPE HCC sample were performed using NanoString's GeoMx DSP as previously described.⁴¹ In brief, 4 μm -thick FFPE tissue sections were treated with a cocktail of 60 uniquely tagged oligonucleotide-labeled primary antibodies. HCC cells and macrophages were identified using anti-panCK and anti-CD68 positive fluorescence imaging, respectively. Guided by this fluorescence imaging, three MCTC⁺ and three MCTC ROIs were selected from each slide for multiplex profiling, spanning a total of seven slides.

For gene transcription analysis, 78 areas of interest (AOIs) from these HCC sections were isolated and examined. In contrast, for protein expression analysis, 24 AOIs from a single HCC section were assessed. Photocleaved oligonucleotides were captured in a microplate and quantified using NanoString's nCounter platform, which decodes the optical barcodes. Collection of oligos from CD68⁺ compartments was prioritized, followed by those from panCK⁺ compartments. In the analytical phase, digital counts were methodically normalized, first against internal spike-in controls, then by the geometric mean of housekeeping genes for each ROI, and finally against IgG isotype controls, to ensure accuracy and reliability of the profiling data.

Genome-wide expression profiling in HCC

For 64 HCC cases within the TJMUCH cohort III, RNA was meticulously extracted from both cancerous tissues and their normal counterparts. We conducted genome-wide expression profiling utilizing the Affymetrix Human Genome U133 Plus 2.0 Array, details of which have previously been reported and are available in the Gene Expression Omnibus (GEO) database under the accession numbers GSE116174 and GSE116182¹⁰. We identified differentially expressed genes between MCTC⁺ and MCTC HCC samples, applying stringent criteria of a fold change greater than 1.5 and a p value less than 0.05. Subsequent pathway enrichment analysis was performed using Gene Ontology (GO) as previously outlined,⁴² providing insights into the biological processes associated with MCTC status.

scRNA-seq and bioinformatic analyses

Single-nucleus RNA sequencing (scRNA-seq) and subsequent bioinformatic analyses were conducted on nuclei isolated from snap-frozen HCC tissues, utilizing a method previously established.⁵² Tissue homogenization was performed on ice using a Dounce homogenizer (Sigma, D9063) with lysis buffer engineered for optimal nuclei preservation. A portion of the resultant homogenate was allocated for bulk RNA isolation, employing the Qiagen RNeasy kit, and subsequently archived at -80°C . The homogenate was then sifted through a 40- μm strainer to procure nuclei, which were further refined using a low-sucrose buffer and gentle sonication. Debris removal was achieved through density gradient centrifugation, employing a 2M sucrose cushion. The isolated nuclei were finally re-suspended in a cold PBS-based solution containing BSA and RNase inhibitor, with integrity and concentration determined via trypan blue exclusion. A benchmark of 1,000 intact nuclei per microliter was set as the standard for progression to scRNA-seq.

The scRNA-seq was executed by LC-Biotechnology, Hangzhou, China. Post-nuclei isolation, 20,000 nuclei per sample were introduced to the 10x Chromium system (10x Genomics), followed by single-nucleus cDNA library construction in accordance with the Chromium Single Cell 3' v3 protocol. Sequencing was performed on the NovaSeq 6000 system, achieving deep coverage with read counts ranging from 33,000 to 106,000 per nucleus on the Illumina HiSeq platform. The dataset has been deposited to the NCBI Gene Expression Omnibus database and the accession number is GSE248907.

Data processing and integration for scRNA-seq were facilitated by Cell Ranger software (v6.0.2), processing gene expression data from the 10x Chromium platform. The human reference genome (GRCh38) was employed for read alignment, and barcode assignment, and unique molecular identifier (UMI) quantification, ensuring comprehensive and accurate transcriptomic profiling. We first filtered out cells with the number of expressing genes <200 or mitochondrial counts $>30\%$. Filtered data were then log normalized and scaled, with cell-cell variation due to UMI counts, and the percentage of mitochondrial reads was regressed out using Scanpy (version 1.9.3). We used the function `scanpy.pp.highly_variable_genes` to selected highly variable genes by setting `max_mean` to 3

and `min_mean` to 0.0125, which are the default values. We used the Harmony⁵³ to remove the batch-effect. We construct K-Nearest Neighbors (KNN) graphs for community detection by Leiden algorithm.⁵⁴ The parameter are as follows: `n_neighbors` = 15 and `resolution` = 1. We employed tSNE to visualize single-cell data.

To define the TAM subtypes, we adopted the classification approach based on marker genes for TAMs as detailed by Ma et al.¹⁹ In their study, Ma et al. synthesized recent scRNA-seq data from tumor research, defining TAM subtypes based on signature genes, enriched pathways, and predicted functions of macrophages. Utilizing this comprehensive summary, we calculated the mean expression values of these signature genes to establish feature scores for each TAM subtype. The signature genes corresponding to each TAM subtype are as follows:

LA-TAMs: ACP5, APOE, APOC1, ATF1, C1QA, C1QB, C1QC, CCL18, CD163, CD36, CD63, CHI3L1, CTSB, CTSD, CTSL, F13A1, FABP5, FOLR2, GPNMB, IRF3, LGALS3, LIPA, LPL, MACRO, MerTK, MMP7, MMP9, MMP12, MRC1, NR1H3, NRF1, NUPR1, PLA2G7, RNASE1, SPARC, SPP1, TFDP2, TREM2 and ZEB1;

Reg-TAMs: CCL2, CD274, CD40, CD80, CD86, CHIT1, CX3CR1, HLA-A, HLA-C, HLA-DQA1, HLA-DQB1, HLA-DRA, HLA-DRB1, HLA-DRB5, ICOSLG, IL-10, ITGA4, LGALS9, MACRO, MRC1 and TGFB2;

Angio-TAMs: ADAM8, AREG, BNIP3, CCL2, CCL4, CCL20, CD163, CD300E, CD44, CD55, CEBPB, CLEC5A, CTSB, EREG, FCN1, FLT1, FN1, HES1, IL1B, IL1RN, IL8, MAF, MIF, NR1H3, OLR1, PPARG, S100A8, S100A9, S100A12, SERPINB2, SLC2A1, SPIC, SPP1, THBS1, TIMP1, VCAN and VEGFA; **Interferon-Primed TAMs (IFN-TAMs):** CASP1, CASP4, CCL2, CCL3, CCL4, CCL7, CCL8, CD274, CD40, CXCL2, CXCL3, CXCL9, CXCL10, CXCL11, IDO1, IFI6, IFIT1, IFIT2, IFIT3, IFITM1, IFITM3, IRF1, IRF7, ISG15, LAMP3, PDCD1LG2, TNFSF10, C1QA, C1QC, CD38, IL411, ISG15, TNFSF10 and IFI44L; **Inflammatory Cytokine-Enriched TAMs (Inflam-TAMs):** CCL2, CCL3, CCL4, CCL5, CCL20, CCL3L1, CCL3L3, CCL4L2, CCL4L4, CXCL1, CXCL2, CXCL3, CXCL5, CXCL8, G0S2, IL1B, IL1RN, IL6, INHBA, KLF2, KLF6, NEDD9, PMAIP1, S100A8, S100A9 and SPP1; **Proliferating TAMs (Prolif-TAMs):** CCNA2, CDC45, CDK1, H2AFC, HIST1H4C, HMGB1, HMGN2, MKI67, RRM2, STMN1, TOP2A, TUBA1B, TUBB and TYMS.

RNA extraction and real-time quantitative PCR (RT-qPCR)

We performed RNA extraction, RT-qPCR as previously described.⁵⁵ RT-qPCR was performed using SYBR Premix Ex Taq Kit (Takara), according to the manufacturer's instructions. Data were collected and analyzed using the Light Cycler 480 instrument (Roche). Primers were listed below: Human M2BP forward primer: CAATGGTACT-TCTACTCCCGAA; Human reverse primer: GAACTGTAG GCAGAGCTTCTC; Mouse M2BP forward primer: CTTCTCGTGTACCTCTAACGAG; Mouse M2BP reverse primer: CTGTTCTCAT AGCCAATTGTCG; The internal reference gene for M2BP was β -actin. The relative expression levels for each sample were calculated based on the $2^{-\Delta\Delta C_t}$ method.

Live-cell imaging assay

1×10^5 HCC cells, transfected with GFP (green fluorescent protein), were seeded in 6 cm culture dishes. Following adhesion, 1×10^6 THP1-derived macrophages were added to the culture. The system was then treated with $1 \mu\text{M}$ GB1107 (MedChemExpress, Cat# HY-114409). Using a live-cell imaging system, the macrophages adhering to the periphery of the tumor cells were observed. Quantitative assessments were conducted at 0 and 24 h post-treatment.

Migration assay

Migration assays were conducted using 24-well plates. A total of 500 μL containing 1×10^5 HCC cells were placed in the lower chamber, while 200 μL containing 5×10^4 THP1-derived macrophages were applied to the upper compartment of the inserts. The system was supplemented with $1 \mu\text{M}$ GB1107. Post a 24-h incubation period at 37°C within a CO₂ incubator, the inserts were collected and stained with crystal violet as previously described.⁵⁶

Cell adhesion assay

The cell adhesion assay was executed using 24-well plates. Each well was inoculated with 1×10^6 HCC cells and incubated at 37°C for 24 h to establish a cell-coated surface. THP1-derived macrophages were labeled with Cell Tracker Red CMTPX Dye (Invitrogen, Cat# C34552) for 30 min, followed by removal of the culture medium. Subsequently, 3×10^5 of the stained macrophages were dispensed into each well along with $1 \mu\text{M}$ GB1107. The plates were then incubated for 24 h at 37°C to facilitate adhesion of the cells to the HCC cell monolayer. Post-washing, the cells that remained adhered to the monolayer were imaged and quantified using a fluorescence microscope.

Immunohistochemical staining

Immunohistochemical staining was performed employing the avidin-biotin-peroxidase complex method. The intensity and distribution of positive staining were assessed using a standardized semi-quantitative dual scoring system as previously detailed.⁴⁶ We utilized a primary antibody against M2BP (Abcam, Cat# ab217760) and incubated at 4°C overnight. Negative controls, which excluded the primary antibody, were incorporated into all experimental procedures.

Quantification of metastatic nodules in subcutaneous tumors

Lung tissues from mice were excised and subsequently embedded in paraffin for sectioning, following a protocol delineated in a previous study.⁵⁷ Serial sections of 5 μm thickness were cut from each lung tissue block. To ensure representative sampling throughout the entire lung, after each section was collected, a set number of consecutive sections (usually 20–40, depending on the tumor nodule size) were skipped before procuring the next. This systematic sampling process was carried out along the entirety of each lung. Metastatic nodules were identified and enumerated on each HE stained section using microscopy. The cumulative count from these sections represented the total number of lung metastatic nodules.

Analysis of immune cell infiltration in subcutaneous tumors

Tumor specimens were processed into single-cell suspensions through enzymatic dissociation, utilizing collagenase IV (GlpBio, Cat# GC19591) at 1 mg/mL and DNase I (GlpBio, Cat# GC19804) at 50 $\mu\text{g/mL}$, as detailed in a previous publication.⁵⁶ The resulting cell suspensions were filtered through a 70- μm strainer (BD Falcon, Cat# 352350) to eliminate debris and then subjected to erythrocyte lysis. Cellular viability was assessed using the Zombie Aqua Fixable Viability Kit (Biolegend, Cat# 423101), distinguishing live/dead cells. Two panels of fluorochrome-conjugated antibodies were utilized in flow cytometry to profile distinct immune cell populations. The first panel was designated for macrophage identification and included PE/Dazzle 594 anti-mouse F4/80 (Biolegend, Cat# 123146), PE anti-mouse/human Mac-2 (Biolegend, Cat# 125405), PE/Cyanine7 anti-mouse CD86 (Biolegend, Cat# 105013), APC anti-mouse CD206 (Biolegend, Cat# 141707), and FITC anti-mouse TREM2 (Invitrogen, Cat# MA5-28223). The second panel targeted T cell markers, comprising PerCP/Cyanine5.5 anti-mouse CD3 ϵ (Biolegend, Cat# 155616), FITC anti-mouse CD4 (Biolegend, Cat# 116003), APC/Cyanine7 anti-mouse CD8a (Biolegend, Cat# 100713), PE anti-mouse FOXP3 (Biolegend, Cat# 126403), Brilliant Violet 421 anti-mouse PD-1 (Biolegend, Cat# 135217), APC anti-mouse LAG-3 (Biolegend, Cat# 125209) and PE/Cyanine7 anti-mouse CD39 (Biolegend, Cat# 143805).

MIF staining followed the aforementioned procedures, with tumor sections incubated with anti-pan Cytokeratin (Abcam, Cat# ab7753), anti-F4/80 (Cell Signaling Technology, Cat# 70076), and anti-CD8 (Cell Signaling Technology, Cat# 98941) antibodies.

QUANTIFICATION AND STATISTICAL ANALYSIS

The statistical analyses were performed with SPSS 16.0 and GraphPad Prism 8. Two-tailed Student's t-tests were used to determine mean differences between two groups. Two-sided Chi-square tests were conducted to compare the difference in rate between two groups. two-way ANOVA was used to compare differences among multiple groups. The Kaplan-Meier method was used to calculate OS and RFS rates, and the log rank test was used to analyze the difference between the survival curves. The Cox proportional hazards regression model was employed for univariate and multivariate analyses to verify the independent risk factor. MedCalc software was used to analyze the results of ROC curve. Statistical significance was determined as indicated in the figure legends. p values of less than 0.05 were considered significant; * $p < 0.05$, ** $p < 0.01$, and *** $p < 0.001$.